MILLIMETERWAVE PHOTOCONDUCTIVITY SPECTROSCOPY IN TWO-DIMENSIONAL ELECTRON SYSTEMS

by

Michael A. Zudov

A dissertation submitted to the faculty of
The University of Utah
in partial fulfillment of the requirements for the degree of

Doctor of Philosophy

Department of Physics

The University of Utah

August 1999

THE UNIVERSITY OF UTAH GRADUATE SCHOOL

SUPERVISORY COMMITTEE APPROVAL

of a dissertation submitted by

Michael A. Zudov

This dissertation has been read by each member of the following supervisory committee and by majority vote has been found to be satisfactory.

	Chair: Rui-Rui Du
	Michael Raikh
	John Worlock
	Bill Sutherland
	Laurence Sadwick

THE UNIVERSITY OF UTAH GRADUATE SCHOOL

FINAL READING APPROVAL

To the Graduate Council of the University of Utah:

I have read the dissertation of Michael A. Zudov in its final form and have found that (1) its format, citations, and bibliographic style are consistent and acceptable; (2) its illustrative materials including figures, tables, and charts are in place; and (3) the final manuscript is satisfactory to the Supervisory Committee and is ready for submission to The Graduate School.

Date

Rui-Rui Du
Chair: Supervisory Committee

Approved for the Major Department

Valy Vardeny
Chair

Approved for the Graduate Council

David S. Chapman
Dean of The Graduate School

ABSTRACT

A new experimental technique, the *Millimeterwave Photoconductivity Spectroscopy*, has been developed and subsequently employed in studies of magneto-excitations near the Fermi surface of a high-mobility *GaAs-AlGaAs* two-dimensional electron system (2DES). Such low-energy magneto-excitations include high-order cyclotron modes and magneto-plasmon modes in a 2DES subjected to a weak perpendicular magnetic field at low temperature.

Higher-order cyclotron modes, forbidden in zeroth-order approximation, reveal themselves as giant amplitude oscillations in millimeterwave photoresistance. It is shown that qualitatively the effect can be explained in terms of beats of Shubnikov-de Haas oscillations, as if there were two Fermi surfaces separated by a radiation quantum. The scattering time τ_{CR} derived within the framework of this model is shown to well exceed Shubnikov-de Haas scattering time τ_{SdH}. This result is attributed to the different roles played by the electron density inhomogeneity in these two regimes. We also emphasize that regular transmission measurements reveal only the cyclotron resonance at the fundamental frequency with no features corresponding to high-order transitions.

In addition, a distinct peak detected in photoresistance is shown to obey the dispersion law of low-frequency magneto-plasmon modes. The finite momentum transfer q needed to excite the 2D plasmon corresponds to a cut-off wavelength given by the width of the sample. It is demonstrated that magneto-plasmon modes can be viewed as standing waves in a 2D waveguide defined by the Hall bar mesa.

To my wife Snezhana, my Mom and my Dad

CONTENTS

LIST OF FIGURES

LIST OF TABLES

ACKNOWLEDGMENTS

I am deeply indebted to my thesis advisor, Professor Rui-Rui Du, for the continuous guidance and support, for his concern and creating a stimulating atmosphere for research.

Special thanks owe to Dr. Jerry Simmons and Dr. John Reno at Sandia National Labs for expert sample preparation.

I am very grateful to Professor Michael Raikh for numerous discussions throughout this research. Thanks also go to Professors Emmanuel Rashba, John Worlock and Bill Sutherland for their support in the course of my study.

This work has been supported by the National Science Foundation.

I acknowledge the University of Utah Graduate Research Fellowship for providing financial support.

Finally I want to thank my family and friends in Salt Lake who helped me to carry out this research.

CHAPTER 1

INTRODUCTION

Electronic nanostructures, fabricated by modern materials techniques, provide exciting opportunities both for fundamental studies and potential applications. Recent developments in device fabrication technology have allowed the creation of semiconductor structures in which electron motion is restricted to a two-dimensional (2D) plane. Electrons in such structures are referred to as a two-dimensional electron system (2DES) or a two-dimensional electron gas (2DEG). The motion of 2D electrons is of a great current interest because nowadays electronic devices have been aggressively approaching ever smaller size and therefore reduced physical dimensionalities at which point the behavior of an electron is governed by its quantum-mechanical nature. Extensive research on the quantum phenomena in confined semiconductors, such as ours, continues leading to many innovations in electronic devices. As examples, we mention electronic devices based on the action of a single electron ("single electron transistor") and that of an electron spin ("spin transistor"). Far-reaching technical applications such as quantum computing and communication may also be proven to rely on our understanding of novel, low-dimensional semiconductor structures.

High quality 2DES are also known as quantum Hall systems due to the fact that remarkable phenomena called integer and fractional quantum Hall effects (IQHE, FQHE) [1, 2] are observed in these structures at high magnetic fields and low temperatures. The presence of strong magnetic field causes a quantization of electron energy resulting in a discrete spectrum of so-called Landau levels (LL) which is similar to that of a simple harmonic oscillator. As dictated by quantum mechanics, electrons will occupy LLs, separated by cyclotron energy, up to the

Fermi level. Since the interlevel spacing is controlled by magnetic field the discrete nature of the spectrum can be detected in magnetotransport.

Transport and electrodynamical properties of 2DES have been at the forefront of the condensed matter physics research over the past two decades [3, 4]. While IQHE can be understood in a single-particle approach, electron-electron interactions are necessary to account for a more complex FQHE. In particular, a great deal of attention has been focused on the physics of the lowest Landau level (LLL), an electron state which occurs when applied magnetic field is strong enough to effectively freeze the kinetic energy of electrons. In this regime electron-electron interactions govern the electron motion and peculiar features appear in transport known as fractional states. One of the major issues here is related to the half-filled Landau level which is presently being examined in terms of the composite fermion (CF), a novel entity which is the bound state of an electron and two Chern-Simons flux quanta which is formed by virtue of electron-electron interactions [5, 6]. The behavior of CFs in many respects is surprisingly similar to that of regular electrons in low magnetic field as has been manifested in an increasing number of experiments. Geometric resonance [7, 8], magnetic focusing [9, 10] and surface acoustic wave (SAW) [11] measurements have now demonstrated the existence of a well-defined Fermi wave vector and semiclassical trajectories for CFs. On the other hand, activation energy [12] and Shubnikov-de-Haas [13] measurements determined effective cyclotron gaps around half-filling being about one order of magnitude smaller as compared to those for regular electrons. These experiments have confirmed that FQHE can be treated as IQHE of composite fermions, and therefore a natural question arises concerning whether one can pursue spectroscopic measurements in this regime.

To date, however, the information on the energetics of CFs has been obtained almost entirely by means of temperature-dependent DC magnetotransport [12, 13] which conceptually pertains to zero frequency ω and a large range of wave vector q. Little is known about their electrodynamical response to a high ω, finite q probing field which is believed to yield information complementary to DC transport measurements. The relevant energy of CF excitations is dictated by the Coulomb

interaction, and is typically in the range of 1 to $10K$, as implied by theory and magnetotransport studies [3, 4].

Established spectroscopic techniques have been historically developed for band electrons and therefore the energy of interest has been in the far-infrared (FIR). In most cases the energy of the probing electro-magnetic field $\hbar\omega$ has been comparable to the Fermi energy ϵ_F of the 2DES which is typically of the order of 10^2K. For example, dynamical measurements of the cyclotron (CR) [14, 15] and magnetoplasmon resonances (MPR) [16, 17, 18] in a 2DES have been traditionally performed by employing FIR spectroscopy [19] with energies above $10cm^{-1}(15K, 300GHz)$. This implies that studies were mostly limited to the situation when only few LLs were occupied neglecting the case of high LLs. On the other hand, recent advances in CF theory and supporting transport studies suggest that energies relevant for CF excitations are in the millimeterwave frequency range. This explains the fact that only recently have spectroscopic measurements in the low-energy regime, *i.e.*, millimeterwave frequencies, become available [20, 21].

Traditional spectroscopy is based upon transmission measurements. Here a bolometer positioned behind the illuminated sample senses the changes in transmitted power due to sample absorption. An alternative approach is photoconductivity in which one measures changes in sample resistance caused by the incident radiation field. Photoconductivity in 2DES has been first successfully employed in electron-spin resonance (ESR) experiments [22] which demonstrated that it has several advantages over traditional transmission spectroscopy. Photoconductivity is relatively simple to implement since utilizing the sample as a detector makes it fully compatible with standard magnetotransport. In addition, photoconductivity may be more sensitive as compared to conventional transmission techniques, especially in case of small 2D samples. Nevertheless, it has not become widely accepted as an experimental tool. This may be due to the fact that there is no existing theory that deals with photoconductivity in realistic samples, and therefore the interpretation of the experimental results may be difficult. Traditionally, however, the photoresistance peak is associated with resonant absorption and the width is

used to extract scattering time [22]. Comparison with transmission measurements which was not possible in ESR studies may provide a further insight on how the absorption translates into the resistivity change.

In this thesis we address the questions regarding the detection of low-frequency collective magnetoexcitations in a quantum Hall system. Our experiments go beyond both the traditional magnetotransport and magnetoabsorption by employing an innovative *Millimeterwave Photoconductivity Spectroscopy* technique developed during this project.

After this introductory chapter we continue with Chapter 2 reviewing the basic physical concepts needed to understand the physics of 2DES. These include a brief description of a typical sample structure, the single-particle energy spectrum of a 2DES in a perpendicular magnetic field, and 2D magnetoplasma dispersion. We also present an overview of various DC transport phenomena such as quantum Hall and Shubnikov-de-Haas (SdH) effects.

Chapter 3 is entirely devoted to the motivation for our *Millimeterwave Photoconductivity Spectroscopy* experiment based on the analysis of energy scales in 2DES and comparison of existing spectroscopic and DC transport techniques.

Details of the experiment are briefly described in Chapter 4. Here we discuss the design of the millimeterwave optical/magnetotransport system, based on the OXFORD ^3He refrigerator equipped with a superconducting magnet. We also present the details on differential lock-in detection, data collection and samples used in this project.

In Chapter 5 we present the results of the *Millimeterwave Photoconductivity Spectroscopy* experiment, including the detection of low-frequency magneto excitations appearing as giant photoresistance oscillations in weak magnetic field. Oscillations are examined in terms of high-order cyclotron resonance (CR), *i.e.*, millimeterwave-induced transitions between not-neighboring LLs. It is nontrivial to observe the high-order transitions since corresponding matrix elements vanish in this case. As has been shown in high magnetic field absorption measurements, even the second order transition is rather weak [14]. However, in our case of low-magnetic

field we have reliably detected CR up to 10^{th} order. It turns out that in this regime where LLs are strongly mixed, a plausible explanation can be given in terms of beats of Shubnikov-de Haas oscillations [23]. We also discuss our experimental results on temperature and density dependence of the oscillations amplitudes. Another type of low-frequency magnetoexcitations detected in our setup is 2D magnetoplasmon, which manifests itself in magnetoresistance as a distinct peak. We show that in our Faraday configuration setup it can be viewed as a standing wave in a 2D waveguide defined by the Hall bar mesa. We conclude Chapter 5 with the discussion of the results obtained by means of conventional transmission spectroscopy.

In Chapter 6 after the conclusions to *Millimeterwave Photoconductivity Spectroscopy* in 2DES we discuss possible implication of the developed technique to the case of composite fermions. Here we address the questions regarding Kohn's theorem and CF scattering time.

In Appendix A we illustrate experimentally the advantages of the developed differential double-modulation photoconductivity technique over traditional realizations.

In Appendix B we present the results on the standard DC magnetotransport experiment where low-field magnetoresistance oscillations beyond SdH effect have been detected in a narrow temperature window around $5K$. The origin of these oscillations remains unclear at this point; two possible scenarios will be considered. Observed oscillations can be phenomenologically explained in terms of the high-order magneto acoustic phonon resonance (MAPR). Being completely free from adjustable parameters and providing good agreement with experimental data, this mechanism, deserves serious examination. However, it is based on a picture of $2k_F$ acoustic phonon scattering which is known to cease in finite magnetic field. Another scenario is based on a picture of a geometric resonance (GR) in a *triangular antidot superlattice*. However there exists no known mechanism for the formation of such a superlattice in a plain 2DES.

CHAPTER 2

PHYSICAL BACKGROUND

2.1 *GaAs-AlGaAs* Heterostructure

High-quality 2DES can be realized on the interface of two semiconductors, namely $GaAs$ and $AlGaAs$. Very small mismatch of lattice constants makes these materials nearly ideal for molecular beam epitaxy (MBE) fabrication of heterostructures with almost defect-free interface. A schematic representation of such a structure is presented in Figure 2.1. It is seen that the conduction band (as well as the valence band) profile simulates a triangular potential well in the z direction. $AlGaAs$ side is usually δ-doped with Si at distance d_S of about several hundred angstroms from the interface. Donated electrons migrate to the interface and form an inversion layer of the width of about $50 - 100$ angstroms. The sheet electron density n is mainly determined by a dopant density N_d and the spacer thickness d_s, and is fixed for a given sample. For instance, in our samples EA100, N_d of the order $10^{12} cm^{-2}$ and $d_s = 700$Å result in electron density n of about $2 \times 10^{11} cm^{-2}$. Recalling that for spin-unpolarized case in two dimensions the Fermi wave-number k_F is equal to

$$k_F = \sqrt{2\pi n} \tag{2.1}$$

one can estimate the Fermi energy ϵ_F:

$$\varepsilon_F = \frac{\hbar^2 k_F^2}{2m^*} \tag{2.2}$$

ε_F is about $80K$ for $n = 2 \times 10^{11} cm^{-2}$ which is considerably smaller than the

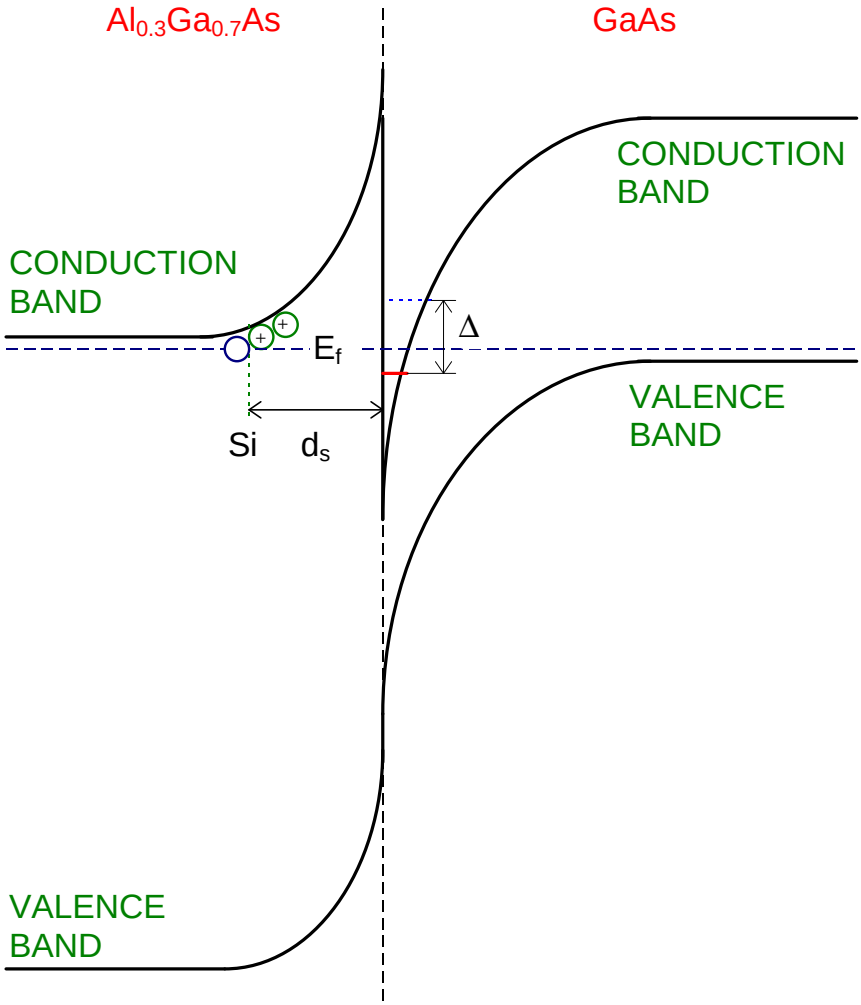

Figure 2.1. GaAs-AlGaAs heterostructure

size-quantization of the well Δ (typically $\sim 200K$). Therefore at low temperature electrons occupy only the lowest subband of the potential well. Due to the separation of the ionized impurities from the interface, where electrons reside, electron scattering is greatly reduced. This results in higher mobility μ as compared to other realizations of 2DES such as Si inversion layer. Our sample EA100 yields low-temperature mobility $\mu = 3.0 \times 10^6 cm^2/V \cdot s$ after a brief illumination from a red light-emitting diode during the cooling process.

Material parameters for the host material, $GaAs$, some of which are used for analysis of experimental data are presented in Table2.1.

2.2 Classical Magnetotransport in 2DES

Classical theory of 2D magnetotransport [24] is based on a concept of a mean free time τ_t (also called transport scattering time). In this picture an electron moving with Fermi velocity $\mathbf{v}_F$ will acquire a drift velocity $\Delta\mathbf{v}$ with the direction and value governed by applied weak electric field

$$\Delta\mathbf{v} = -\frac{e\mathbf{E}\tau_t}{m^*} = -\mu\mathbf{E} \tag{2.3}$$

where μ is an electron mobility:

$$\mu = \frac{e\tau_t}{m^*}. \tag{2.4}$$

Table 2.1. Material parameters for GaAs

Energy gap, E $(T = 4.2K)$	$1.52eV$
Lattice constant, a	5.64Å
Electron effective mass, m^*	$0.068m_0$
Dialectric Constant, ϵ $(\omega \to 0)$	12.8
Electron g-factor, g	-0.44
Velocity of sound, u_s	$2.88km/sec$

Taking into account that in the presence of magnetic field the electron path is curved due to Lorenz force $-e\mathbf{v}\times\mathbf{B}$, Ohms law can be written as

$$\mathbf{j}=\sigma_0\mathbf{E}-\sigma_0\frac{\mathbf{j}\times\mathbf{B}}{ne} \tag{2.5}$$

where n is the sheet electron density and σ_0 is the conductivity at zero magnetic field given by a Drude formula

$$\sigma_0=\frac{ne^2\tau_t}{m^*}=ne\mu \tag{2.6}$$

Now, if one assumes that electrons are confined to the (x,y) plane and magnetic field is applied along z-direction, i.e. $\mathbf{B}=(0,0,B)$, then the resistivity tensor can be written as follows:

$$\widehat{\rho}=\begin{pmatrix}\rho_0 & B/ne\\ -B/ne & \rho_0\end{pmatrix},\ \rho_0=\frac{1}{\sigma_0} \tag{2.7}$$

Conductivity tensor $\widehat{\sigma}$ is a matrix inverse of $\widehat{\rho}$

$$\widehat{\sigma}=\widehat{\rho}^{-1}=\begin{pmatrix}\sigma_{xx} & \sigma_{xy}\\ \sigma_{yx} & \sigma_{yy}\end{pmatrix} \tag{2.8}$$

$$\sigma_{xx}=\sigma_{yy}=\frac{\sigma_0}{1+\omega_c^2\tau_t^2};\ \sigma_{xy}=-\sigma_{yx}=\frac{ne}{B}+\frac{\sigma_{xx}}{\omega_c\tau_t} \tag{2.9}$$

The discovery of quantum Hall effect [1] in 1980, however, showed that not only quantum-mechanical treatment of the problem is essential but also one needs to account for localization-delocalization processes in high magnetic field.

2.3 Energy Spectrum of 2DES

To find an energy spectrum of 2DES let us write Schrödinger equation for spinless noninteracting electrons in the presence of magnetic field

$$\frac{\hbar^2}{2m^*}\left\{\left[-i\frac{\partial}{\partial x}-\frac{eB}{\hbar}\right]^2-\frac{\partial^2}{\partial y^2}\right\}\cdot\Psi(x,y)=E\cdot\Psi(x,y) \tag{2.10}$$

Here we use the Landau gauge for the vector potential $\mathbf{A}$

$$A_x=-yB,\ A_y=0 \tag{2.11}$$

After some manipulations $\left(\Psi\propto e^{ikx}\varphi(y)\right)$ we obtain a shifted harmonic oscillator equation

$$\frac{\hbar\omega_c}{2}\left\{-l_0^2\frac{d^2}{dy^2}+\left[\frac{y}{l_0}-l_0k\right]^2\right\}\cdot\varphi(y)=E\cdot\varphi(y) \tag{2.12}$$

where we have introduced magnetic length

$$l_0=\sqrt{\frac{\hbar}{eB}} \tag{2.13}$$

which is an intrinsic length scale of the system. The eigenvalues for harmonic oscillator equation are well known and quantum number $N=0,1,2,...$ defines the so-called Landau levels:

$$E_N=\hbar\omega_c\left(N+\frac{1}{2}\right) \tag{2.14}$$

Taking into account electron spin, each LL is split into two separated by Zeeman energy

$$E_{N,\pm}=\hbar\omega_c\left(N+\frac{1}{2}\right)\mp\frac{1}{2}\mu_B gB \tag{2.15}$$

where μ_B is Bohr magneton and g is the electron g-factor. Signs $+(-)$ correspond

to spin-down(up) branches of electrons. Therefore one concludes that, in an ideal 2DES, energy spectrum consists of Landau levels separated by cyclotron gaps $\hbar\omega_c$ which are further spin-split with Zeeman energy $\mu_B g B$.

Now let us write down the density of states (DOS) n_B of a single level which is just the ratio of the applied magnetic field B to the flux quantum Φ_0

$$n_B = \frac{1}{2\pi l^2} = \frac{eB}{h} = \frac{B}{\Phi_0} \tag{2.16}$$

and introduce an electron filling factor ν defined as the ratio of electron density n to the DOS n_B

$$\nu = \frac{n}{n_B} \tag{2.17}$$

It is easy to see that ν is just the number of occupied levels. Schematic representation of the energy spectrum for a filling factor $\nu = 8$ is shown in Figure 2.2. Fermi level is shown by a dashed line located in the gap between 4^{th} and 5^{th} LLs. Since the number of states in a single level is proportional to applied magnetic field, filling factor ν scales linearly with inverse magnetic field $1/B$.

2.4 Integer Quantum Hall Effect

Integer quantum Hall effect (IQHE) was discovered by Klaus von Klitzing [1] who found that at low temperature for some finite ranges of magnetic field, in the vicinity of *integer* filling factors $\nu \approx i$, the conductivity tensor takes the following form

$$\widehat{\sigma}_{QHE} = \begin{pmatrix} 0 & i \cdot e^2/h \\ -i \cdot e^2/h & 0 \end{pmatrix} \tag{2.18}$$

As seen from Equation 2.18 IQHE manifests itself in a step-like behavior of the Hall conductivity $\sigma_{xy}(= -\sigma_{yx})$ as a function of a perpendicular magnetic field. Plateaus

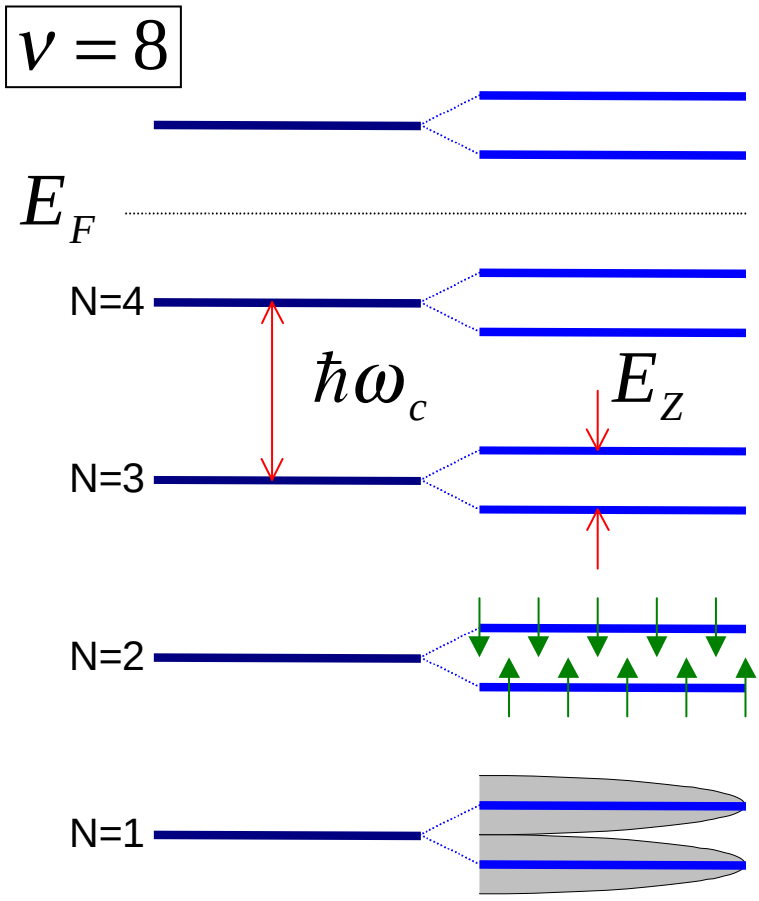

Figure 2.2. Energy spectrum of 2DES for $\nu = 8$

are developed at the quantized values of conductivity precisely at the positions $i \cdot (e^2/h)$, where i is an *integer*. This quantization condition on the plateaus is found to be obeyed with an extreme accuracy. At the same time, the longitudinal conductivity $\sigma_{xx}(= \sigma_{yy})$ becomes zero in the plateau regions and exhibits sharp maxima centered at the values of magnetic field at which the Hall conductivity experience steps.

To get some qualitative explanation of this phenomenon it is important to notice that in a real system there is always a certain amount of disorder which modifies the spectrum. It is believed that not all states in LLs are extended; localized states exist in cyclotron gaps (see Figure 2.2). The role of localized states is crucial since they allow the Fermi level to sit between LLs for some finite range of magnetic field. Under such conditions the current carried by the extended states is not affected. Phenomenologically, experimental observations can be interpreted if one takes a limit of the conductivity tensor $\widehat{\sigma}$ (see equation 2.9) as scattering time τ_t tends to infinity:

$$\lim_{\tau_0 \to \infty} \left(\frac{\sigma_0}{1 + \omega_c^2 \tau_t^2} \right) = 0 \tag{2.19}$$

$$\lim_{\tau_0 \to \infty} \left(\frac{ne}{B} + \frac{\sigma_{xx}}{\omega_c \tau_t} \right) = i \frac{e^2}{h} \tag{2.20}$$

It is important that this situation occurs for finite ranges of magnetic field at $\nu \approx i$ where the Fermi level lies in the gap.

2.5 Shubnikov-de Haas Oscillations

As the magnetic field decreases, extended states centered at LLs start to overlap and localized states do not play important role anymore. Spin-splitting is not resolved in low magnetic fields due to small g-factor in $GaAs$ (see Table 2.1). As a result, the density of states becomes a continuous periodic function of inverse magnetic field and IQHE is replaced by SdH oscillations [25]. Practically, the formalism for SdH oscillations can be applied for 2D case [26, 27, 28]. According

to this formalism, an amplitude of oscillations normalized to the zero-field ($B = 0$) resistance R_0 follows the expression

$$\frac{\Delta R}{4R_0} = \frac{A_T}{\sinh(A_T)} \exp(-\pi/\omega_c\tau), \tag{2.21}$$

$$A_T = \frac{2\pi^2 kT}{\hbar\omega_c} \tag{2.22}$$

Detailed analysis of this expression is provided in Section 3.2.

2.6 Fractional Quantum Hall Effect

In an extremely clean 2DES additional quantization in energy spectrum appears due to strong electron-electron interaction thus leading to a more peculiar *fractional* quantum Hall effect (FQHE), discovered by Tsui, Stormer and Gossard in 1982 [2]. Contrary to IQHE, FQHE is phenomenologically characterized by the fact that the Hall conductivity σ_{xy} has quantized plateaus not at the integer filling factors ($\nu \approx i$) but at certain simple *rational fractions* ($\nu \approx f = p/q$) where q is always odd. The most prominent series of FQHE states is observed at filling factors converging to half-filling ($\nu = 1/2$):

$$\nu \approx f = \frac{p}{2p \pm 1} = \frac{1}{3}, \frac{2}{5}, \frac{3}{7}, ...; \frac{2}{3}, \frac{3}{5}, \frac{4}{7}... \tag{2.23}$$

Recalling that the filling factor ν is just the number of filled LLs, we see that for $\nu < 1$ all the electrons are confined to the LLL. In other words, cyclotron motion of electrons is frozen out by the strong magnetic field. It is thus clear that single-particle energy spectrum discussed in Section 2.3 can not account for FQHE in any respect. Here, electron-electron correlations play a key role since there is only one energy scale, namely Coulomb interaction of two electrons at an average distance given by the magnetic length l_0 (see Equation 2.13).

Since the discovery of FQHE there have been a variety of theoretical studies trying to explain this unique many-electron phenomenon. First successful attempt

was made by Laughlin [29] in 1983 who proposed a trial wave function to describe the ground state at the primary filling factor $\nu = 1/m$, m odd

$$\Psi_{1/m} = \prod_{j<k} (z_j - z_k)^m \cdot \exp\left(-\frac{1}{4}\sum_l |z_l|^2\right) \tag{2.24}$$

Here z is an electron coordinate in a complex plane, *i.e.*, $z = x + iy$. It was shown later in finite size studies that this function is indeed an extremely good approximation for the exact ground state [4]. The energy required to create a fractionally charged quasiparticle corresponds to an energy gap in the spectrum. Similarly to a cyclotron gap in IQHE, this quasiparticle gap is responsible for the Hall quantization and dissipasionless transport at this primary filling factor $\nu = 1/m$.

Soon after the primary filling factors were explained, the hierarchy scheme was proposed [30, 31] to explain other fractions. It was postulated that quasiparticle excitations of the Laughlin state form a next level Laughlin-like state to produce a new fraction. However, it was noticed that not only all the fractions are phenomenologically identical to each other but they are also experimentally quite similar to integers. Therefore it was very attractive to build a theory treating all the fractions on the same footing and providing their, at least intuitive, comparison to integers. The resulting theoretical understanding of the FQHE is based on a concept of the composite fermion [5], the new particle which appears from a Chern-Simons gauge transformation [6]. A system of electrons interacting with each other in a complex fashion via Coulomb repulsion is thus transformed into a system of new weakly interacting quasiparticles. In the simplest case of the most prominent fractions the composite fermion is formed out of electron and two magnetic flux quanta. CFs have the same charge, spin and statistics as the regular electrons and experience a reduced effective magnetic field which is offset by a value of magnetic field at electron filling factor $\nu = 1/2$ where the Chern-Simons flux of CFs exactly compensates the external magnetic flux [6]

$$B_{eff} = B - 2n\Phi_0 = B - B_{1/2} \tag{2.25}$$

At exactly half-filling, CFs move in an apparently zero *effective* magnetic field in spite of the presence of an extremely high *external* magnetic field. As a result, highly degenerate Fermi liquid emerges at half filling with a Fermi wave vector k_F^{CF} related in a simple manner to that of the electrons in zero magnetic field:

$$k_F^{CF} = \sqrt{2}k_F \tag{2.26}$$

where k_F is given by Equation 2.1. Filling factor of CFs p is written by analogy with an electron filling factor ν (see Equation 2.17) with the total magnetic field B replaced by a reduced effective field B_{eff}

$$p = \frac{n\Phi_0}{B_{eff}} \tag{2.27}$$

It is important to note that according to this picture FQHE of electrons at the filling factor ν is equivalent to IQHE of composite fermions at the filling factor p. Therefore it seems appropriate to introduce empirically an effective mass of CFs relating energy gaps in the spectrum to the corresponding cyclotron gaps $\hbar eB_{eff}/m_{CF}^*$. Since m_{CF}^* is a measure of an electron-electron interaction and the only energy scale is the Coulomb energy governed by the magnetic length l_0, CF effective mass depends on the applied magnetic field as $m_{CF}^* \propto \sqrt{B}$ contrary to an electron mass.

Another important conclusion is that electron filling factor $\nu = 1/2$ corresponds to zero effective field of CFs ($B_{eff} = 0$) and by analogy with electrons at zero magnetic field one expects the formation of a well-defined Fermi surface and metallic behavior of the CF system. Numerous experimental studies have shown later on that under certain circumstances CFs indeed behave surprisingly similar

to electrons in weak magnetic field. Among those are billiard-type experiments probing semiclassical trajectories of CFs, such as surface acoustic wave (SAW) [11], geometric resonance (GR) on antidot arrays [7, 8] and magnetic focusing [9, 10] experiments.

A series of successful magnetotransport studies around filling factor $\nu = 1/2$ was performed in order to measure m^*_{CF} [13, 12] confirming that FQHE can be viewed as IQHE of CFs. These include SdH and activation energy experiments which reveal the value of m^*_{CF} to be about one order of magnitude larger as compared to electron effective mass, $m^*_{CF} \sim 10m^*$.

Moreover, it was observed in transport studies in tilted magnetic fields [32, 33] around filling factor $\nu = 3/2$ that CFs carry spin and the corresponding g-factor g_{CF} is about the same as that for regular electrons.

2.7 Two-Dimensional Magnetoplasma

Two-dimensional (2D) plasmons are low-frequency collective oscillations of an electron density. Their dispersion law is gapless in the absence of magnetic field, in contrast to a three-dimensional (3D) case. The frequency of 2D plasmon ω_P tends to zero in long-wavelength limit $q \to 0$ where $\mathbf{q} = (q_x, q_y)$ is the wave vector of a 2D plasmon. This may be understood if one consider fluctuations of the electron charge density in the form of periodically (with period $2\pi/q$) placed charged planes (3D) or lines (2D). The restoring force responsible for plasma oscillations does not depend on the period in 3D case and decreases inversely proportionally to the period in two dimensions. Therefore ω_P^2 does not depend on q for the bulk case, and $\omega_P^2 \sim q$ for 2D plasmon. In general, the dispersion law of 2D plasmon may be found from the zeros of the effective longitudinal dielectric permittivity of a 2D system: $\varepsilon(q, \omega) = 0$. In the simplest approximation that ignores nonlocal interactions ($ql_0 \geq 1$), the dispersion of a long wavelength ($\omega/c < q \ll k_F$, where k_F is the Fermi wave vector) plasmon is known [17, 34, 35] to be:

$$\omega_P^2(q) = \frac{ne^2 q}{2\epsilon\epsilon_0 m^*} \tag{2.28}$$

where ϵ is the effective dielectric function of the surrounding media. In the presence of a perpendicular magnetic field, the plasmon has a low cut-off frequency given by the cyclotron frequency $\omega_c = eB/m^*$ and the coupled cyclotron-plasmon modes or magnetoplasmon (MP) dispersion then becomes

$$\omega_{MP} = \sqrt{\omega_c^2 + \omega_P^2}. \tag{2.29}$$

The MP dispersion dictates that MP resonances can be observed only by coupling to a finite momentum transfer q, usually via a spatially modulated radiation field or electron density.

Also one has to mention that theoretical study of magnetoplasma in a strip geometry [36] gives the following dispersion

$$\omega_{Pk}^2(q) = \frac{ne^2\pi k}{2\epsilon\epsilon_0 m^* w} \tag{2.30}$$

where w is the width of the strip and $k = 0, 1, 2, ...$ This allows the excitation of MP modes when half-integers of the MP wavelength commensurate with the sample width which were observed in quantum wires. Under certain conditions such modes can be also viewed as standing waves at a cut-off wavelength defined by the width of a 2D strip.

CHAPTER 3

MILLIMETERWAVE SPECTROSCOPY IN 2DES

3.1 Energy Scales in 2DES

In this chapter we present the motivation for our *Millimeterwave Photoconductivity Spectroscopy* experiment. To justify the choice of millimeterwave radiation as a probe, we provide a brief review of relevant energy scales present in a 2DES.

Cyclotron resonance (CR) of 2D electrons can be studied in the absence of the magnetic quantization effects, even in a very weak magnetic field when Landau splitting is not resolved. Cyclotron motion in magnetic fields of the order of $0.1T$ yields cyclotron energy of about $2K$ which falls into the millimeter wave frequency range ($1K \approx 20GHz$). As far as spin motion is concerned, it has much smaller energy scale as compared to cyclotron energy (see Table 3.1). For detection of the electron-spin resonance (ESR) high magnetic field is important since it is desirable to have all electrons in the LLL. In this case employing the millimeter wave frequency is also very natural. In addition to that, under certain conditions the frequency of plasma oscillations falls into millimeter wave frequency range. For example, the dispersion law (see Equation 2.30) applied to our Hall bar sample EA100HB of the lithographic width $w = 200\mu m$ yields plasma frequency ω_P of about $50GHz$. All phenomena mentioned above may already justify the choice of millimeter wave radiation as a probe for weak magnetic field excitations since this frequency range has not been employed (with the exception of the ESR). However, the principal motivation for our research was to study interaction effects dominating in the extreme quantum limit.

Table 3.1. Energy scales in 2DES

Size quantization of the well, Δ	$200K$
Fermi energy, ε_F $(n = 2.0 \times 10^{11} cm^{-2})$	$80K$
Coulomb energy, E_c $(B = 10T)$	$160K$
Cyclotron energy, $\hbar\omega_c$ $(B = 0.1T)$	$2K$
Zeeman energy, E_z $(B = 10T)$	$3K$
2D Plasmon, $\hbar\omega_P$ $(q = 3 \times 10^4 cm^{-1})$	$2K$
CF Cyclotron energy, $\hbar\omega_c^*$ $(B_{eff} = 1.0T)$	$2K$

As was discussed in Section 2.6 in FQHE regime when all electrons are confined to LLL the kinetic energy is frozen out by the magnetic field and the Coulomb repulsion plays important role. In magnetic field of $10T$, magnetic length l_0 is about 80Åleading to a Coulomb energy of $160K$. Energies for magneto-excitations are determined by the Coulomb energy which is the only energy scale in LLL. For example, both theoretical [3] and experimental [12] studies of the $\nu = 1/3$ gap energy converge to $\Delta_{1/3} = 0.1e^2/\epsilon l_0$. In the CF picture FQHE gaps are directly related to the effective mass of composite fermions m^*_{CF}. From temperature-dependent transport studies it is known that effective field of $1T$ corresponds to the excitation energy of about $2K$. Summary of the relevant energy scales is presented in Table 3.1.

3.2 Standard Magnetotransport in 2DES

Transport in magnetic fields is a well-established tool to study electronic structures in 2DES. Its implications are based on the fact that electron density of states at the Fermi level varies with magnetic field. Variations of the density of states can be detected via changes in the sample resistance. Measurements are traditionally performed by means of low-frequency lock-in detection which is described in Section 4.1. Important parameters such as carrier density n, effective mass m^*, scattering times τ_t, τ_{SdH} and g-factor g can be extracted from magneto-transport.

As an example, let us consider a case of a weak magnetic field where resistance exhibit SdH oscillations discussed in Section 2.5. Typical experimental trace for sample EA100HB is shown in Figure 3.1.

The period of oscillations is dictated by a ratio of the Fermi energy ε_F to the cyclotron energy $\hbar\omega_c$ from which we can easily extract electron density n taking into account Equation 2.2. Scattering time τ_{SdH}, in turn, can be extracted from a damping exponential (see Equation 2.21) if one plots the amplitude of the oscillations versus inverse magnetic field (Dingle plot). Finally, effective mass m^* can be measured from temperature dependence of the oscillation amplitudes.

At higher magnetic fields where SdH formula is no longer valid, the energetics of the system is traditionally probed via activation energy measurements. Here, by varying the temperature, carriers are excited across the energy gap and the longitudinal resistivity exhibits exponential temperature dependence according to equation

$$\rho_{xx}(T) \propto \exp(-\Delta/2kT) \tag{3.1}$$

Here, Δ is the gap in the electron energy spectrum if one disregards effects of disorder. If, for example, the activation energy experiment is performed on IQHE states with even filling factor, the gap Δ is just equal to the cyclotron gap $\hbar\omega_c$ and therefore effective mass m^* is readily available. However, in some cases, effect of disorder is important and may result in overestimating the electron effective mass.

Being relatively simple, standard magneto-transport technique proved to be a very powerful tool to study the excitation energies of electrons and in many experiments was successfully applied to the more complicated case of composite fermions.

On the other hand, standard DC transport is not a spectroscopic tool (with the exception, for example, tunneling spectroscopy). The millimeterwave spectroscopy described in this thesis provides useful information supplementary to the standard DC transport results.

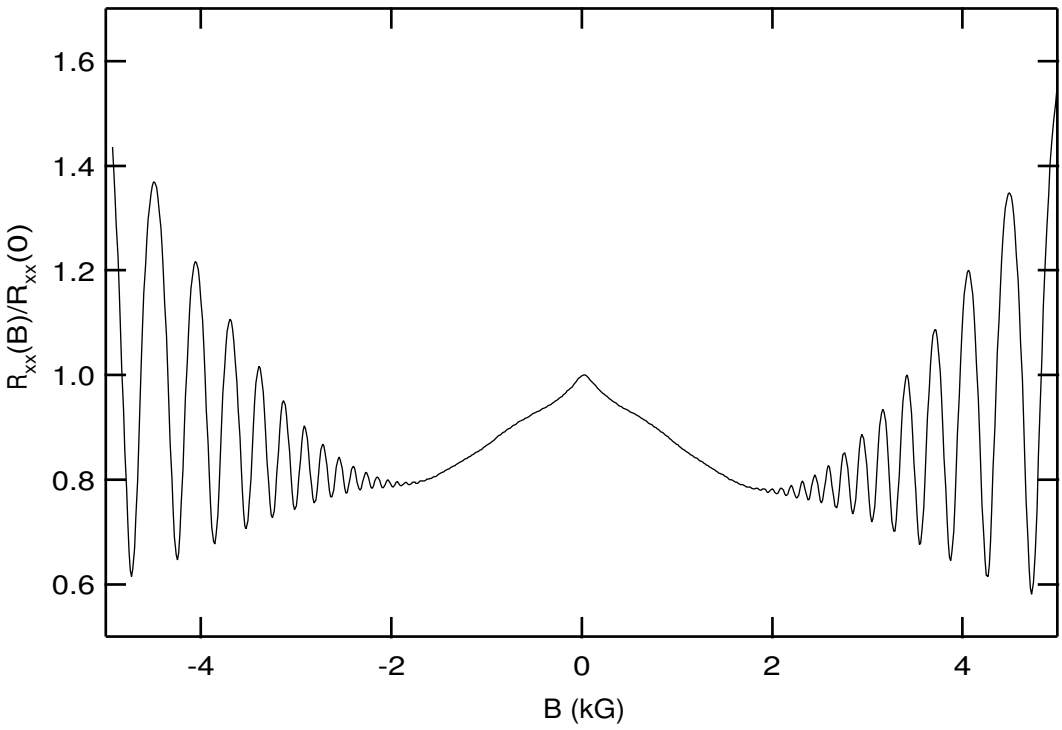

Figure 3.1. Shubnikov-de Haas oscillations in sample EA100HB

3.3 Resonant Magnetoabsorption in 2DES

A direct method to probe the energy spectrum in 2DES is to introduce a new energy scale into 2DES. The standard experimental technique is called resonant magnetoabsorption. In this approach the sample subjected to a perpendicular magnetic field is illuminated by electro-magnetic radiation. A bolometer placed behind the sample is used to detect the transmittance changes when the system resonates with radiation.

As an example, let us consider a simple first-order cyclotron resonance. If one sweeps magnetic field while illuminating the sample with monochromatic radiation, the sample will absorb the radiation when the cyclotron frequency ω_c coincides with the frequency of the millimeter wave radiation ω. This situation occurs when Landau splitting becomes equal to the energy of incident photon, *i.e.*,

$$\hbar\omega_c = \hbar\omega \tag{3.2}$$

The absorption coefficient α is given by real part of classical (Drude) conductivity

$$\alpha = \frac{1}{2} Re\left[\sigma_+(\omega) + \sigma_-(\omega)\right], \quad \sigma_\pm(\omega) = \frac{i \cdot \sigma_0}{(\omega \mp \omega_c) + i/\tau} \tag{3.3}$$

where σ_0 is Drude conductivity given by Equation 2.6. In Figure 3.2 we plot the absorption coefficient a versus magnetic field B for radiation frequency $f = 94GHz$ and selected values of scattering time τ of $5ps$, $10ps$ and $20ps$ which are represented by dashed, dotted and solid lines respectively. This illustrates relatively strong dependence of the CR detectability on the sample quality.

The position of the maximum which satisfy resonant condition (3.2) yields information on effective electron mass m^* and the width is related to scattering time τ. Thus by fitting the experimental data with an expression in Equation 3.3 one can extract both m^* and τ. However, no information can be gained on the Fermi wave vector k_F since cyclotron frequency ω_c has no dependence on electron density n.

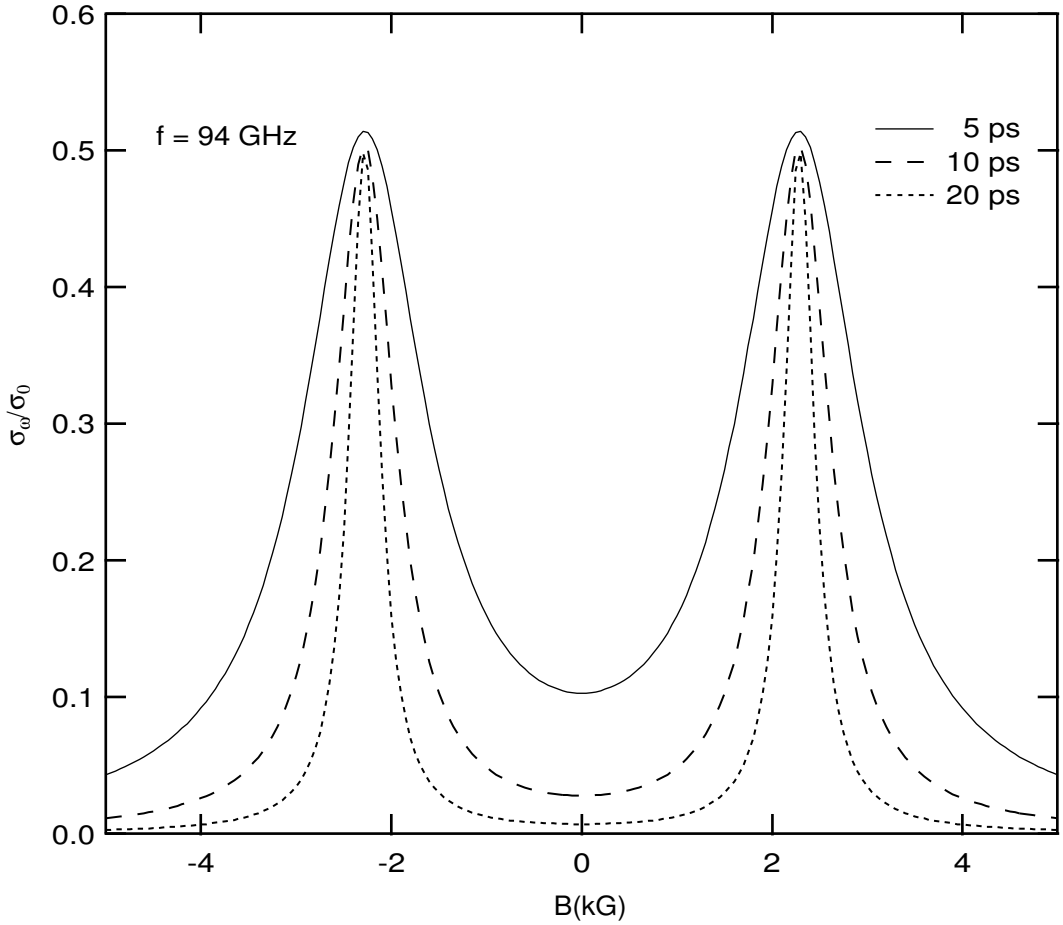

Figure 3.2. Magnetoabsorption in 2DES for radiation frequency $f = 94GHz$

3.4 Resonant Photoconductivity in 2DES

The main idea behind *Millimeterwave Photoconductivity Spectroscopy* was to combine standard magneto-transport with magnetoabsorption. In the simplest realization of this experiment we measure magnetoresistance as it is done in standard magneto-transport but under continuous microwave illumination. As will become clear in Section 5.2, by virtue of a new energy scale given by a radiation quantum, both the Fermi wave vector k_F and the effective mass m^* are accessible at the same time.

To date, photoconductivity in 2DEG is not well understood theoretically, especially when translating the absorption of the radiation field to the conductivity. One possible mechanism is related to the resonant delocalization of initially localized carriers, thus leading to the conductivity enhancement. However in a metallic regime, *i.e.*, in low magnetic field, such interpretation fails. In addition, it is expected that inhomogeneous broadening known to suppress quantum oscillations in regular transport does not affect resonant photoconductivity response. This means that non-metallic regime is effectively extended to lower field. Another complication arises from the fact that localization-delocalization processes can not be included perturbatively in any theory and therefore quantitative analysis, such as that of the magnitude and the shape of the photoconductivity peak, is difficult. Nevertheless, the peak in conductivity is traditionally related to resonant absorption. For example, in ESR experiments the width of the photoconductivity peak is used empirically to estimate the spin scattering time [22]. Experimental comparison of the widths and heights of the CR and MPR is possible via standard transmission spectroscopy.

CHAPTER 4

DESIGN AND DETAILS OF EXPERIMENT

4.1 Modulation and Phase-Lock Detection

Simplest lock-in detection which is widely used in standard transport measurements is based on an idea of the excitation current modulation ($I_{ex}\sin(\omega t)$) and subsequent detection of the voltage drop at the modulation frequency ω. The main advantage is signal-to-noise ratio enhancement provided by the fact that only noise in a narrow frequency band around modulation frequency ω affects the measurement. An instrument implementing this technique is called lock-in amplifier which multiplies the measured signal $I_{ex}R\sin(\omega t)$ by internally generated reference signal of the form $\sin(\omega t)$. After the multiplication has taken place, useful signal can be easily extracted by means of a low-pass or *sinc* filtering. The later one simply averages the signal over one period of reference signal thus completely eliminating contributions from higher harmonics. The resulting DC component is referred to as X- or *in-phase* channel. The described lock-in process can be described by the following equations (from now on we switch to notation $x = \omega t$):

$$I_{ex}R\sin(x)\sin(x) = \frac{1}{2}\cdot I_{ex}R\cdot(1-\cos(2x)) \propto \frac{1}{2}\cdot I_{ex}R \tag{4.1}$$

for the case of low-pass filtering and

$$\frac{1}{2\pi}I_{ex}R\int_0^{2\pi}\sin(x)\sin(x)dx = \frac{1}{2}\cdot I_{ex}R \tag{4.2}$$

for the *sinc* filtering. Note that both methods give identical results and we will use the last one in the rest of the discussion. Also it is important to mention the ability

of modern lock-in amplifiers to measure simultaneously an *out-of-phase* signal by means of multiplication on $\cos(x)$ instead of $\sin(x)$. The result is referred to as Y- or *out-of-phase* channel and is presented by

$$\frac{1}{2\pi} I_{ex} R \int_0^{2\pi} \cos(x)\sin(x)dx = 0 \tag{4.3}$$

4.2 Single Modulation Technique

Although some modifications are important the basic lock-in technique described above can be readily employed for the case of differential photoconductivity. In this case, as described in Section 3.4, one have to deal with another excitation source, namely millimeterwave radiation. As the name of photoconductivity implies, the desired signal in this case is the change in resistance due to millimeterwave radiation ΔR.

The simplest realization of differential photoconductivity is via DC current excitation (I_{dc}) and chopping the millimeterwave radiation with a square wave. The resistance in this case is also changing in a square wave fashion:

$$R_{mw} = R + \Delta R \cdot \left(\frac{1}{2} + \frac{2}{\pi} \left[\sin(x) + \frac{\sin(3x)}{3} + \frac{\sin(5x)}{5} + ... \right] \right) \tag{4.4}$$

Lock-in detection at the chopping frequency gives the following results for X- and Y-channels respectively:

$$\begin{aligned} \frac{1}{2\pi} I_{dc} \int_0^{2\pi} \sin(x) R_{mw}(x) dx &= \frac{1}{\pi} \cdot I_{dc} \Delta R \\ \frac{1}{2\pi} I_{dc} \int_0^{2\pi} \cos(x) R_{mw}(x) dx &= 0 \end{aligned} \tag{4.5}$$

The X-channel gives the desired signal proportional to ΔR, however this method can not be applied for the following reasons. Millimeterwave field distribution is

not completely uniform along the sample surface and therefore it will necessarily produce some additional voltage drop due to induced photocurrent I_{ph} which, in general, has arbitrary direction. This signal has the same modulation as R_{mw} and therefore will be picked up by lock-in as well. Taking into account the coupling between components of the conductivity tensor, it is easy to see that produced photovoltage most likely will smear out the useful signal, namely $I_{dc}\Delta R$. To illustrate this we assume that photocurrent I_{ph} has the same direction as the driving current I_{dc} and both currents can be added together yielding the equation similar to Equation 4.4:

$$I_{mw}(x) = I_{dc} + I_{ph} \cdot \left(\frac{1}{2} + \frac{2}{\pi} \left[\sin(x) + \frac{\sin(3x)}{3} + \frac{\sin(5x)}{5} + ... \right] \right) \qquad (4.6)$$

This changes Equation 4.5 as follows:

$$\begin{aligned} \frac{1}{2\pi} \int_0^{2\pi} \sin(x) I_{mw}(x) R_{mw}(x) dx &= \frac{1}{\pi} \cdot (I_{dc}\Delta R + I_{ph}(R + \Delta R)) \qquad (4.7) \\ \frac{1}{2\pi} \int_0^{2\pi} \cos(x) I_{mw}(x) R_{mw}(x) dx &= 0 \end{aligned}$$

Therefore one concludes that strong mixing with photovoltage makes this method unacceptable which is demonstrated experimentally in Appendix A.

4.3 Double Modulation Technique

For our photoconductivity experiment we have developed and employed a double modulation technique that allows us to separate the photoresistance $I_{ex}\Delta R$ and photocurrent $I_{ph}(R + \Delta R)$ signals thus virtually eliminating the effects of non-uniformity of the radiation field and at the same time increasing the sensitivity. The key point here is the modulation of both the excitation current and millimeterwave radiation at different frequencies. Modulating signals are synchronized with each other as well as with the reference signal of lock-in amplifier. To simplify the

synchronization process we chose to double the frequency of the excitation current with respect to the modulation frequency of millimeterwave radiation.

In our setup the sample is excited with a current modulated at frequency $2x$ while microwave is chopped with x. Then, as before, R_{mw} is described by Equation 4.4 but I_{mw} is modified as follows

$$I_{mw}(x) = I_{ex}\sin(2x) + I_{ph}\cdot\left(\frac{1}{2} + \frac{2}{\pi}\left[\sin(x) + \frac{\sin(3x)}{3} + \frac{\sin(5x)}{5} + ...\right]\right) \quad (4.8)$$

This changes the Equation 4.7 as follows:

$$\begin{aligned} \frac{1}{2\pi}\int_0^{2\pi}\sin(x)I_{mw}(x)R_{mw}(x)dx &= \frac{1}{\pi}\cdot I_{ph}\left(R+\Delta R\right) \quad (4.9)\\ \frac{1}{2\pi}\int_0^{2\pi}\cos(x)I_{mw}(x)R_{mw}(x)dx &= \frac{2}{3\pi}\cdot I_{ex}\Delta R \end{aligned}$$

In this case signals are naturally separated with the photovoltage appeared on the X-channel and photoresistance on the Y-channel of the lock-in amplifier. Comparing the last of two equations with Equation 4.2 one arrives at an additional scaling factor of $3\pi/4$ which should be used to convert the lock-in reading into $I_{ex}\Delta R$. Similarly to convert to $I_{ph}\left(R+\Delta R\right)$ one should factor the reading by $\pi/2$. The detailed comparison of the techniques based on real experimental situation is provided in Appendix A.

4.4 Experimental Apparatus

Our experimental setup is based on the OXFORD top-loading sorption-pumped ^3He refrigerator/superconducting magneto-transport system. In order to make this system suitable for magneto-optical measurements it has been significantly modified by careful design and painstaking experiments. The major modifications include the integration of the millimeter waveguide designed to transmit linearly

polarized radiation and the optical table on the top of the cryostat to accommodate millimeterwave components. Special care has been taken while integrating waveguide to prevent the base temperature from going up due to additional channel of thermo-coupling to room temperature via the waveguide. In our setup we use thin ($0.010''$) stainless steel waveguide WR-28 designed for frequencies from $28GHz$ to $40GHz$. To minimize the heat load to the ^3He liquid it was properly heat-sinked at $4K$ and $1K$ points. Placing a black polyethylene filter inside the waveguide proved to be sufficient to block the $300K$ black body radiation as well as visible light. By these measures the base temperature raised only about $10 - 20mK$ as compared to the original setup. Sample is placed on a thin ($0.020''$) piece of fiber-glass board located at the end of the waveguide. The orientation of the sample with respect to the waveguide corresponds to Faraday configuration, as shown in Figure 4.1. Care has been taken to place all metal leads necessary for electrical connections outside the waveguide thus preventing the disturbance of the radiation field. To minimize possible interference effects associated with reflections and forming of the standing waves, an adiabatically shaped, graphite absorber was placed inside the waveguide in front of the sample. This also significantly reduces the temperature fluctuations of the ^3He bath produced by the modulated radiation. Such fluctuations, if severe, would be detected in differential photoconductivity as nonresonant heating.

Another major modification was done to allow standard transmission measurements. An $InSb$ bolometer was mounted in the volume of the cancellation coil in the superconducting solenoid. Radiation is transmitted through a wedged sapphire optical window which separates the ^3He liquid and the vacuum space of the bolometer. Indium wires were used to reliably seal the window surface with a stainless steel flange in the ^3He tail. Specially designed gold-plated, brass cone is used to guide the radiation from the illuminated sample down to the bolometer. In order to keep the bolometer temperature stable the cone was thermally decoupled from the ^3He bath via a Teflon spacer. In addition to that bolometer was mounted on a thin ($0.020''$) sapphire plate which was in turn glued to a copper flange. Copper flange was then thermally anchored via a copper wire to the bottom flange of the

inner vacuum chamber. As a result the bolometer was kept at stable temperature of $4K$ regardless of the ^3He bath temperature which was necessarily varied in some of the experiments. Bolometer was carefully checked against linearity of the response.

Schematics of the experimental setup is shown in Figure 4.2. Sample is immersed in ^3He liquid. Pumping on the liquid provides well-controlled temperature range from 0.3 to $2K$. Magnetic field from superconducting magnet up to $14T$ is applied perpendicular to the sample surface, which however may be tilted, if necessary, employing a specially built tilting stage. Coherent, linearly polarized, millimeter wave radiation is provided by a solid state source (11 Gunn oscillators) of tunable frequency which cover the wide frequency range $f = \omega/2\pi$ from 30 to $150GHz$ (1.5 to $7.5K$). The output power of the source (typically from 10 to $100mW$) can be AM or FM modulated and controlled with a 30dB attenuator placed between the source and the waveguide. Frequency meter is used for frequency control and stabilization. Typically, photoresistance trace is recorded at constant temperature, frequency and power of the radiation during the magnetic field sweep.

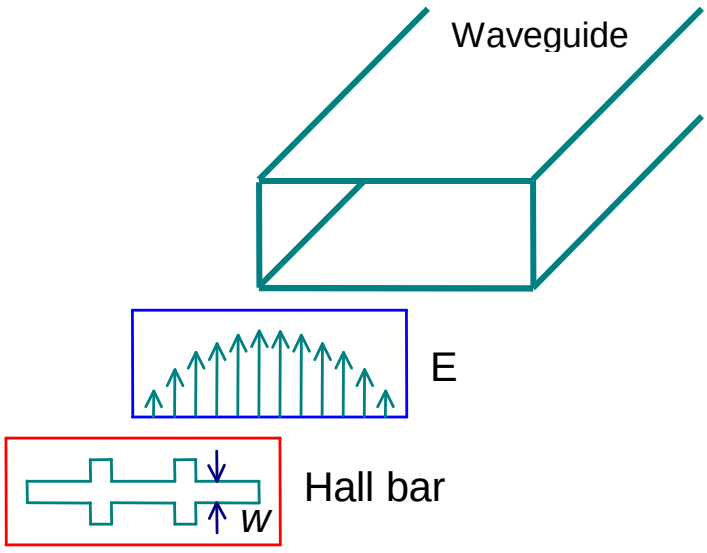

Figure 4.1. Orientation of the sample with respect to the waveguide

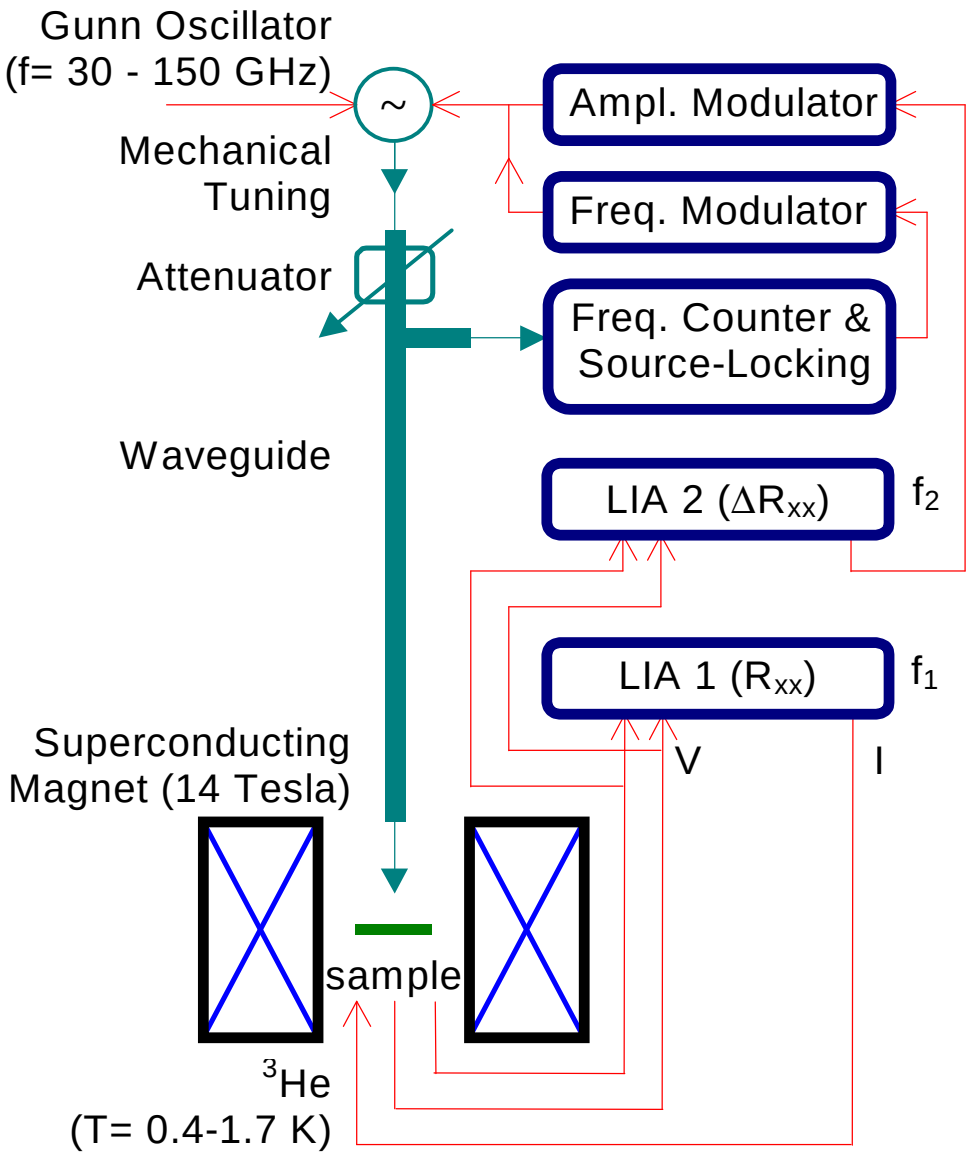

Figure 4.2. Schematics of experimental setup

4.5 Instrument Control and Data Collection

Acquisition of experimental data was performed using Pentium-based PC computer which was interfaced with various instruments via standard NI GPIB/TNT card using IEEE 488.2 protocol. Data acquisition interface, developed using NI Labview and Borland C++ programming environments, allows simultaneous control of up to 32 devices. Due to its built-in universality and expandability instruments can be easily added and removed from the control panel based on the needs of particular experiment. Data are displayed in real time during the magnetic field sweep which is fully controllable via interface.

4.6 Samples

Our samples are high quality MBE-grown *GaAs-AlGaAs* heterostructures, prepared by Dr. J.A. Simmons, Sandia National Laboratories (SNL). The summary of the samples used during this project is presented in Table 4.1. The n and μ are the data after a brief illumination by a light-emitting diode at $\sim 4K$

Here, size of the Hall bar samples represents the width of the mesa. Density in sample EA100GT is controlled via a semi-transparent *NiCr* gate. Samples EA100HB and EA137HB are squares with 8 diffused *In* contacts placed symmetrically along the edge. Hall bar samples have from 8 to 16 *AuGeNi* contacts. The 0.20(0.10)mm mesa is 24(48) squares long which is divided in sections of 2(4), 4(8) and 16(32) squares.

Table 4.1. Sample parameters

Sample name	Configuration	Size, mm	n $(10^{11}cm^{-2})$	μ $(10^{6}cm^{2}/Vs)$
EA137VP	Van der Pauw	6×6	2.17	2.5
EA100VP	Van der Pauw	6×6	2.17	3.0
EA137HB	Hall Bar	0.20	2.17	2.5
EA100HB	Hall Bar	0.20	2.17	3.0
EA100GT	Hall Bar	0.10	$1.1 - 2.5$	–

CHAPTER 5

EXPERIMENTAL RESULTS

5.1 Giant Photoresistance Oscillations

In this chapter we present experimental results, namely on the detection of CR and MPR near the Fermi surface ($\hbar\omega_c \ll \varepsilon_F \approx 80K$) of a high-mobility 2DES by microwave photoresistance measurements. In a high-mobility *GaAs-AlGaAs* 2DES subject to a *weak* magnetic field we observe giant photoresistance oscillations associated with high-order CR, *i.e.*, the resonant transitions between nonadjacent Landau levels. This is an unexpected result. Such transitions have been previously seen in CR experiments in the high magnetic field B regime [14] and have been explained via an analysis of short-range scattering potentials [37]. In the high B limit, however, the amplitude of even the second order CR remains rather small. Our experiments represent another limit, namely the weak B field regime. The dramatic enhancement of the high-order CR observed here is attributed to a strong mixing of many LLs in a weak B field [23].

In Figure 5.1 we show the normalized magnetoresistance $R^{\omega}_{xx}(B)/R^{\omega}_{xx}(0)$ in sample EA100HB under microwave illumination for several values of millimeterwave frequency $f = \omega/2\pi$. The R^{ω}_{xx} is measured by sweeping magnetic field B while f and T are held constant. Without illumination (dotted line), the sample starts to exhibit normal Shubnikov-de Haas (SdH) oscillations at an onset field $B_{SdH} \sim 2.0kG$.

New, giant amplitude magnetoresistance oscillations appear under microwave illumination arising from a correction to the magnetoresistance owing to the resonant absorption of microwave radiation. The correction, or the photoresistance defined as $\Delta R^{\omega}_{xx}(B) = R^{\omega}_{xx}(B) - R^{0}_{xx}(B)$, generally alternates in sign with increasing B. Moreover, it forms an oscillatory structure that is roughly periodic in inverse magnetic field $1/B$ (see *e.g.*, the trace at $45GHz$), similar to SdH oscillations. With

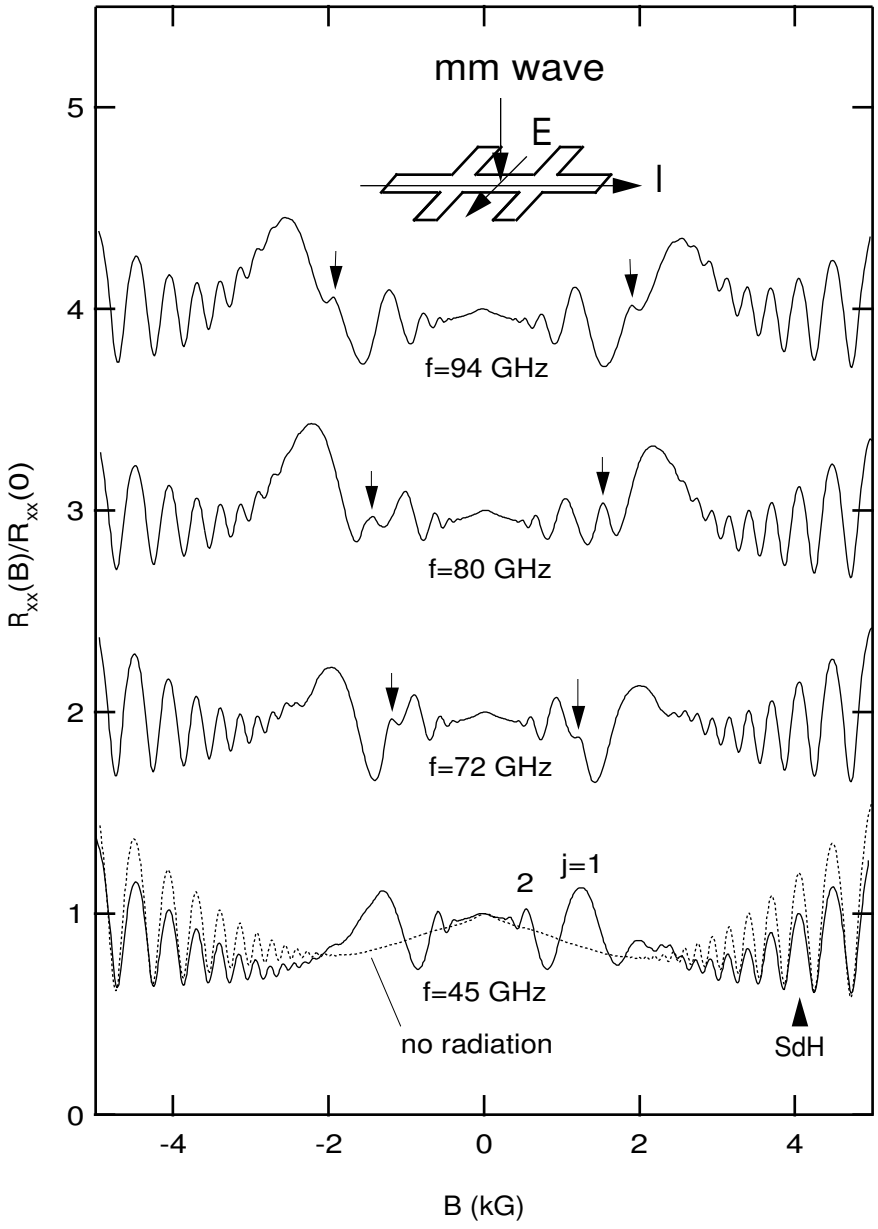

Figure 5.1. Normalized photoresistance in sample EA100HB

increasing f, this oscillatory structure shifts toward higher B in an orderly fashion, *i.e.*, preserving the periodicity, but largely remains limited to a low B range where the SdH effect is absent. On the other hand the number of oscillations, in general, grows with increasing frequency reaching as high as 10 above $100GHz$. More surprisingly yet, a distinct ΔR_{xx}^{ω} peak emerges for frequencies f above $60GHz$, with an amplitude and a width in B comparable to those of the CR features. The B field position of this additional peak shifts from one CR peak toward another as f increases, thus manifesting stronger frequency dependence. This is the MP resonance that is discussed in Section 5.6 of this chapter.

5.2 Electron Effective Mass

Since we have introduced a new energy scale into the system given by the radiation quantum one expects to obtain the information on the energy spectrum of the system. In particular we are able to determine the electron effective mass from the following analysis. For illustration, Figure 5.2 shows a low-field part of magnetoresistance trace for sample EA100HB under continuous microwave illumination of $f = 120GHz$ at $T = 0.4K$.

We see that oscillations persist up to 7th order and resemble Shubnikov oscillations (see Figure 3.1). However, the B positions of the $\Delta R_{xx}^{\omega}(B)$ peaks satisfy a resonance condition in which the microwave quantum equals an *integer multiple* j of the cyclotron energy $\hbar\omega_c = \hbar eB/m^*$

$$\hbar\omega = j \cdot \hbar\omega_c \tag{5.1}$$

or

$$j = \frac{\omega}{\omega_c} \tag{5.2}$$

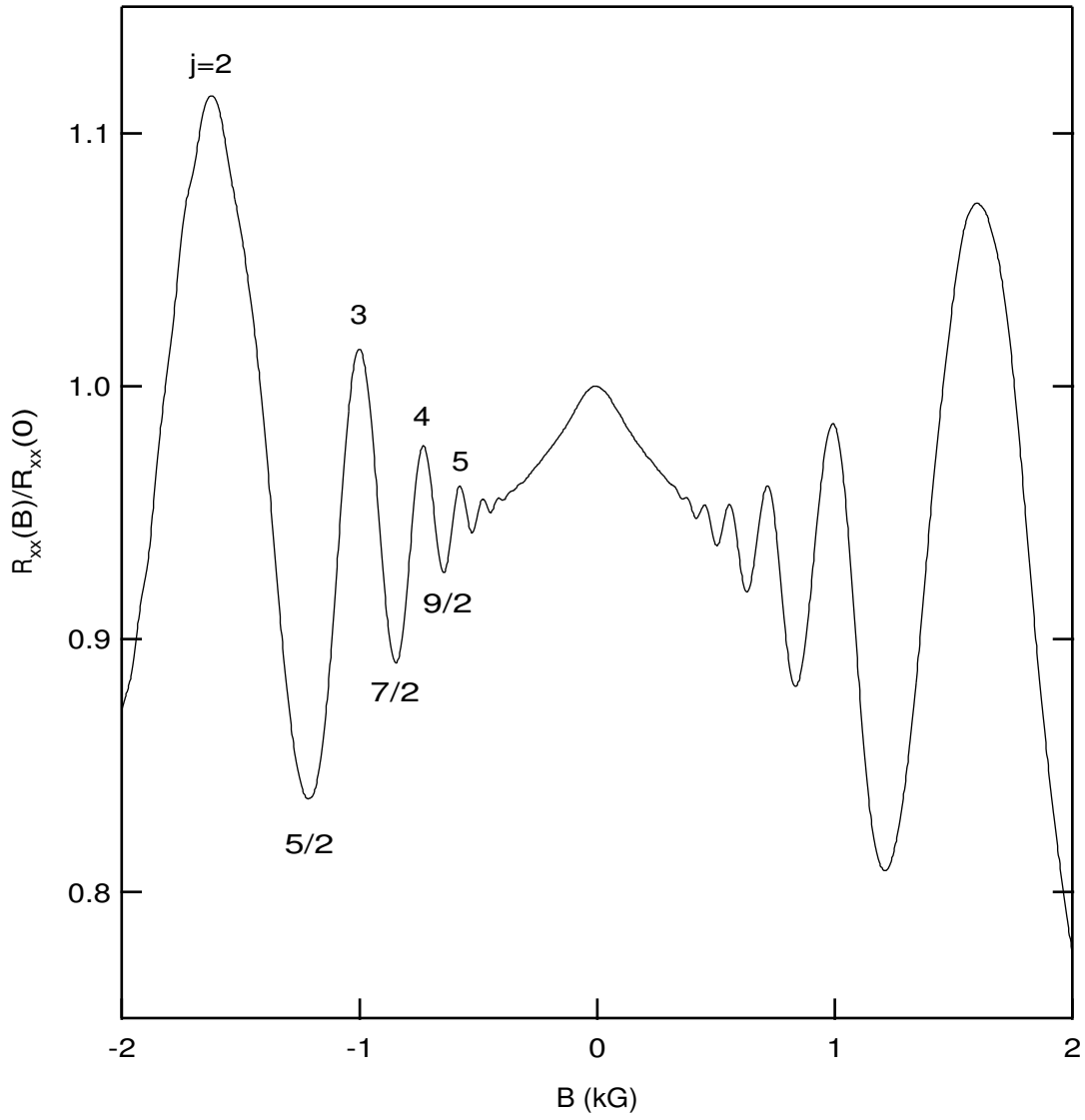

Figure 5.2. Low field part of the typical photoresistance trace for frequency $f = 120GHz$ and $T = 0.4K$

Double modulation technique described in Section 4.3 increases the sensitivity allowing the detection of up to 10 harmonics of CR as shown in Figure 5.3. Here we plot the photoresistance ΔR_{xx}^{ω} in sample EA137HB at $f = 148.5GHz$ and $T = 0.42K$. Another example of enhanced resolution at lower frequency $f = 44GHz$ is shown in Figure 5.4. Both plots demonstrate that oscillations persist down to the onset value of magnetic field $B_{CR} \approx 250G$ which seems to be independent of the radiation frequency. In Figure 5.4 we also plot the absorption line (dotted line, right axis) calculated in accordance with Equation 3.3 using scattering time $\tau_{CR} = 20ps$.

To determine an effective mass we plot in Figure 5.5 the multiplicity index j versus inverse magnetic field $1/B$ for two sets of data. Open symbols correspond to the data shown in Figure 5.2. We also include data from another sample, EA137HB, taken at frequency $f = 44GHz$ and temperature $T = 2.0K$ and represented by solid symbols. Here we include both the integer $j = 2, 3, ...$ (maxima in photoresistance) and the half integer $j = 3/2, 5/2, 7/2, ...$ (minima), since both are described by Equation 5.2. Solid lines are calculated using the corresponding radiation frequencies and an electron effective mass $m^* = 0.068m_0$ in $GaAs$ (see Table 2.1). Excellent agreement for both datasets over the whole range of $j > 1$ is observed. We conclude that detected giant oscillations are due to microwave-induced transitions between nonadjacent LLs, or high-order CR.

5.3 Theory of High-Order CR in Weak Magnetic Field

It is well known that in a simple harmonic oscillator model discussed in Section 2.3 dipole-dipole matrix elements are nonvanishing only for transitions between neighboring energy levels; all other transitions are not allowed. Therefore, the very fact of the observation of high harmonics needs explanation. While high-order CR has been previously observed in high B field [14], the amplitude of even second harmonic remained very weak as compared to the fundamental. It turns out that in low magnetic field regime strong mixing among multiple LLs results in dramatic enhancement of high-order transitions.

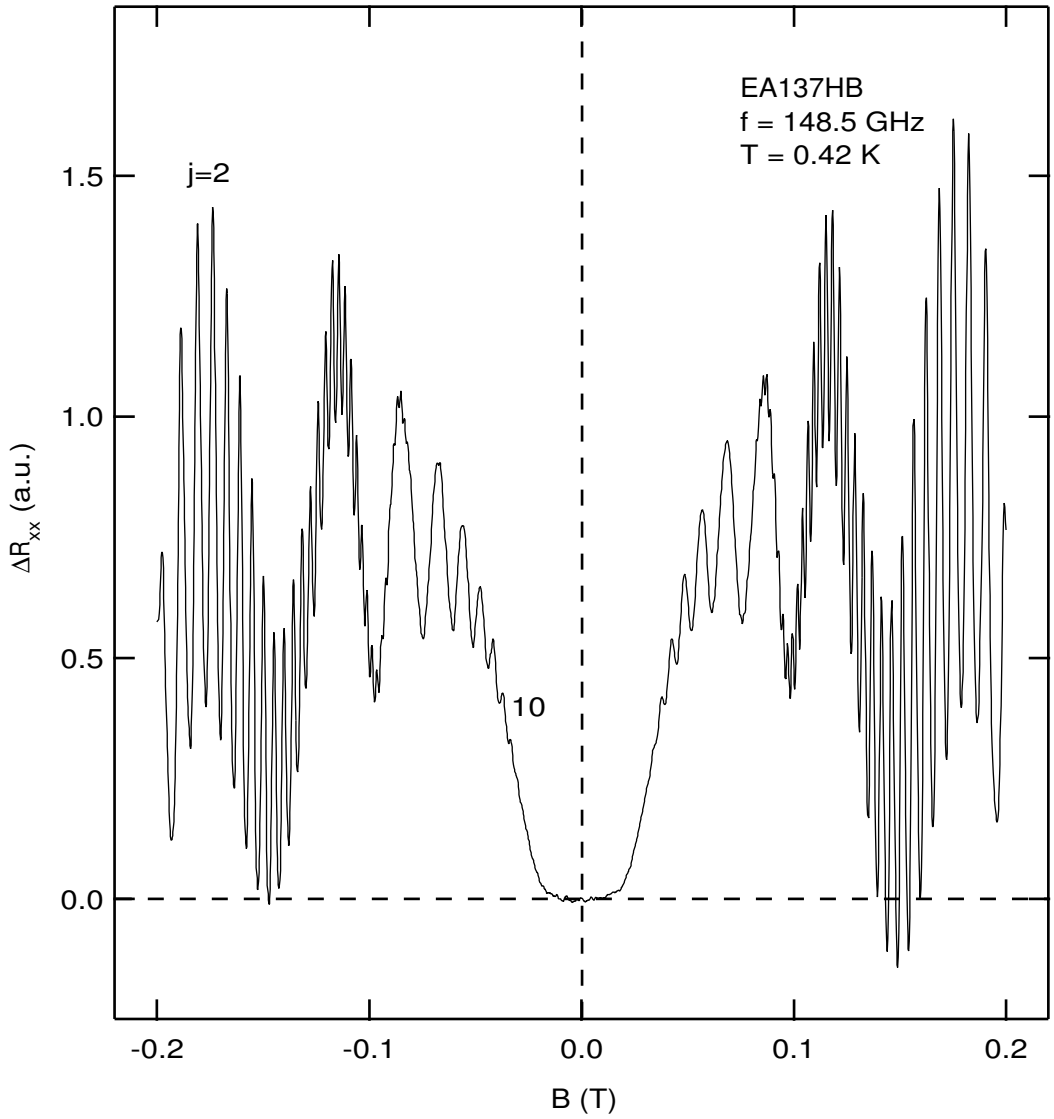

Figure 5.3. Photoresistance measured via double modulation technique in sample EA137HB at $f = 148.5GHz$ and $T = 0.42K$

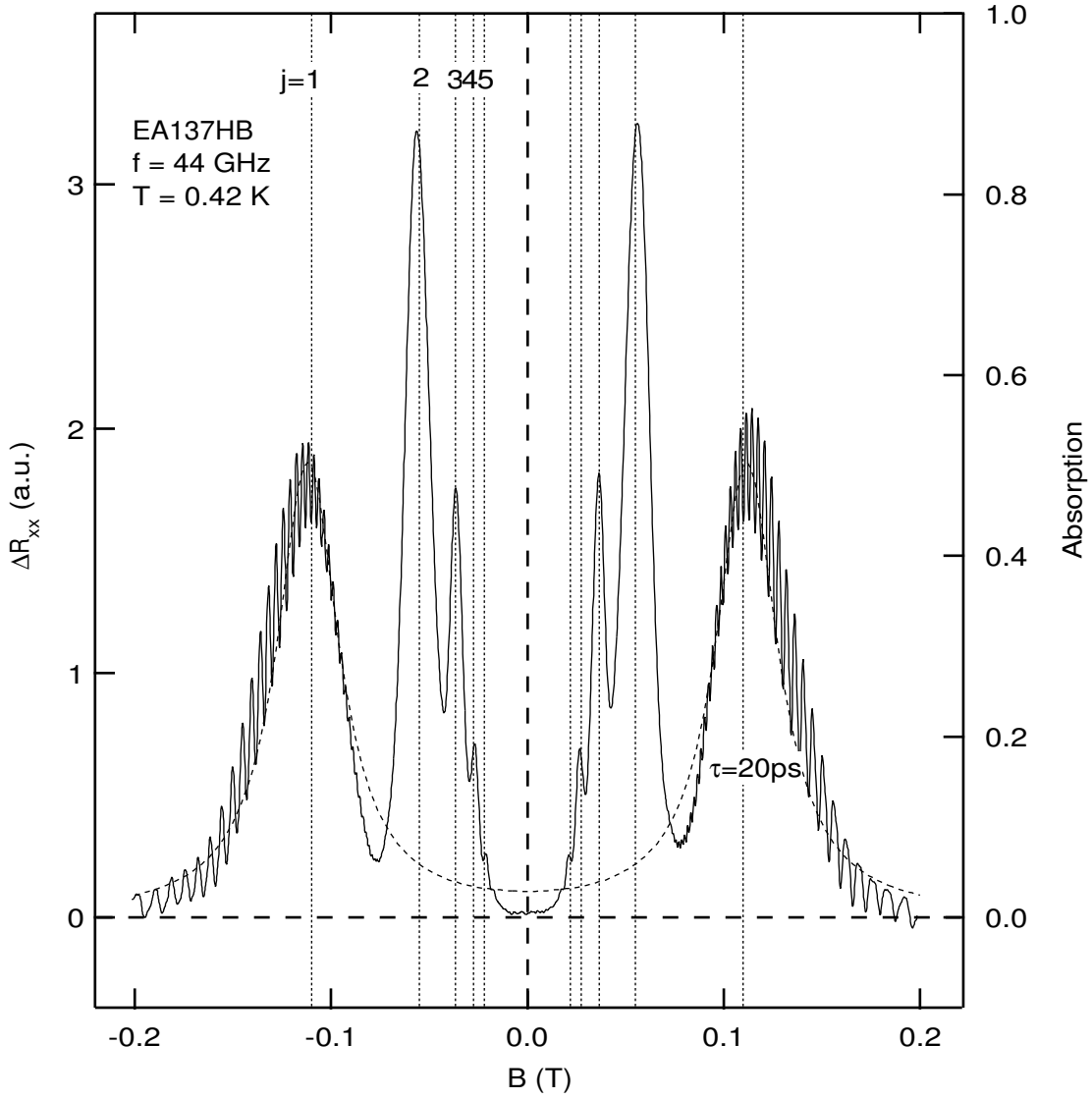

Figure 5.4. Photoresistance measured via double modulation technique in sample EA137HB at $f = 44GHz$ and $T = 0.42K$

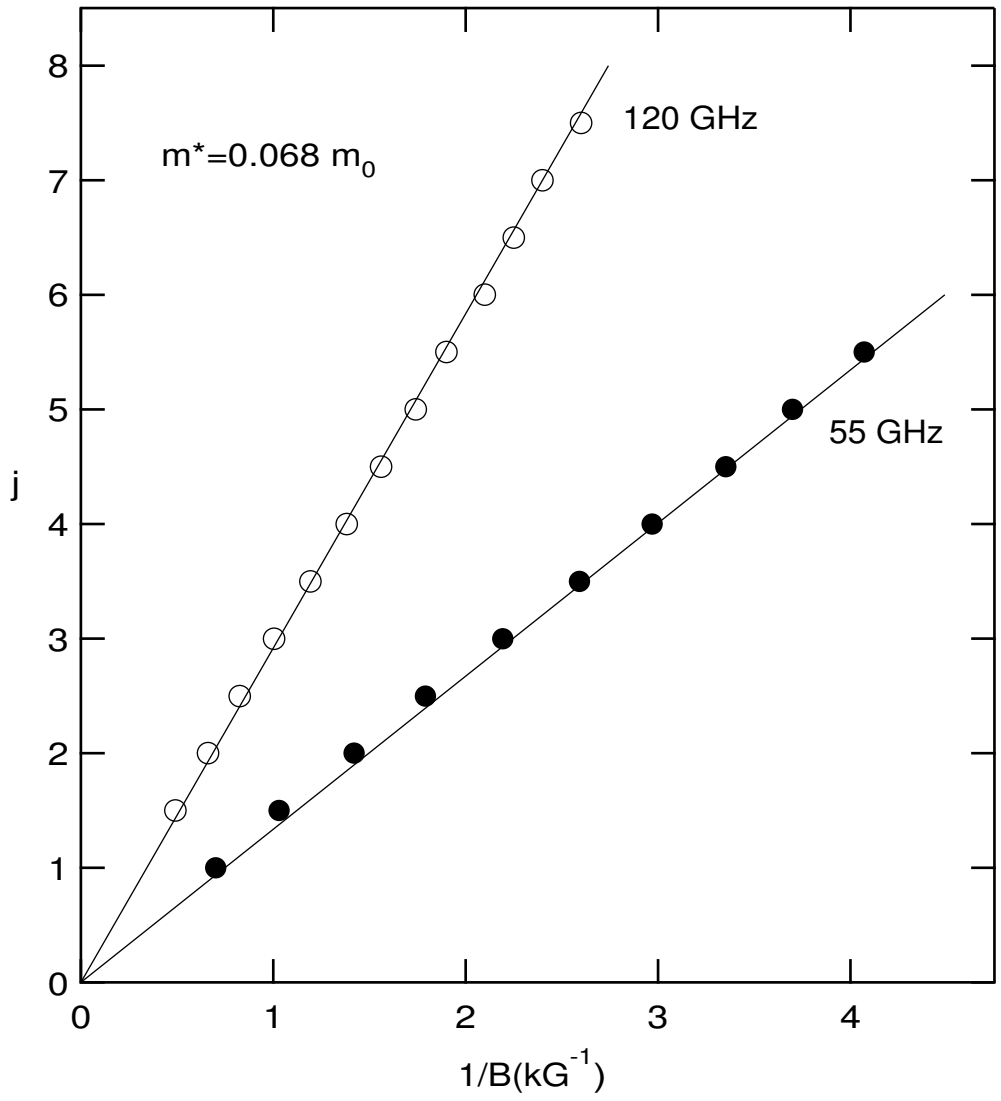

Figure 5.5. Order of the CR j versus inverse magnetic field

The model proposed by Raikh [23] is based on an assumption that in the presence of the radiation LL staircase (see Figure 2.2) splits into two separated by a quantum of the radiation field. As the magnetic field varies in experiment, every time when the resonant condition (5.1) is satisfied two staircases of LLs become perfectly aligned and an electron can scatter from one staircase to another. Appearance of an additional scattering channel at selected values of magnetic field results in increase of resistance thus leading to an oscillatory structure observed in our experiment. In other words, CR oscillations can be viewed as the beats of SdH oscillations originating from different LL staircases and corresponding conductivity corrections can be described by a simplified formula [23]:

$$\Delta\sigma_{xx}(\omega) \propto \cos(2\pi\omega/\omega_c) \cdot \exp(-2\pi/\omega_c\tau). \tag{5.3}$$

Several comments are appropriate here. While such photoresistance oscillations may resemble those arising from SdH effect (see Section 2.5), they differ in the following crucial aspects.

First, the period is controlled by the ratio ω/ω_c rather than $\varepsilon_F/\hbar\omega_c$. Here the absence of the Plank's constant $\hbar$ indicates a purely classical effect. The absence of the Fermi energy ε_F in Equation 5.3 also implies that the effect does not depend on the electron density. This is supported by similar data obtained from other samples of differing density. Also this implies that the effect may be much more tolerable to the density inhomogeneity. This explains the fact that the onset field for giant oscillations of $0.025T$ is much smaller as compared to the SdH value of about $0.1T$.

In addition, the oscillations are expected to have very weak T dependence within a certain temperature range. Indeed, as shown in Figure 5.6, the amplitudes of the CR oscillations do not change significantly from 0.4 to $1.8K$, whereas the SdH exhibits very strong T dependence. This is because the mutual alignment of LL staircases is not affected by temperature and therefore averaging over Fermi distribution has no effect.

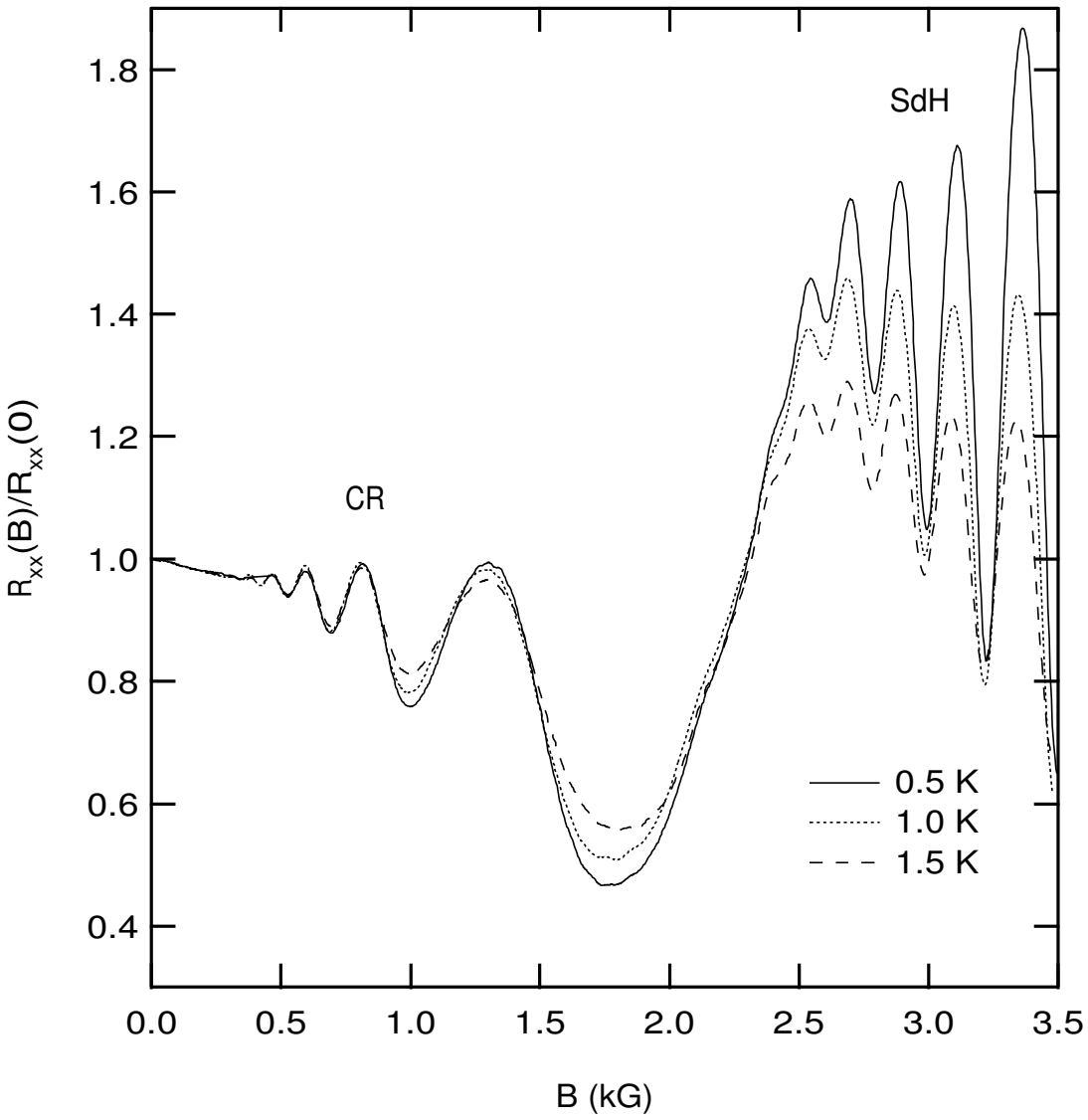

Figure 5.6. Temperature dependence of CR oscillations in sample EA137HB

Finally, the damping exponential in Equation 5.3 contains a factor of 2 as compared to the usual Dingle factor in SdH formalism.

5.4 Scattering Times

In this section we estimate and compare scattering times which are present in the system, namely transport scattering time τ_t, Shubnikov-de Haas scattering time τ_{SdH} and cyclotron resonance scattering time τ_{CR}.

Transport scattering time is determined from the classical theory of magneto-transport (see Section 2.2). Equation 2.4 can be rewritten as $\tau_t = \mu m^*/e$ yielding τ_t of $\sim 115ps$ ($\sim 180ps$) for sample EA100HB (EA137HB).

To estimate SdH scattering time τ_{SdH} we employ a standard Dingle plot procedure. In Figure 5.7 we plot the amplitude of Shubnikov-de Haas oscillations for sample EA137HB at temperature $T = 0.4K$ against electron filling factor ν in a semi-log scale. According to Equation 2.21 we observe a straight line with a slope corresponding to scattering time τ_{SdH}. Least-square fit generates $2.5(2.0)ps$ for sample EA137HB(EA100HB). One can also get an estimate for scattering time from the condition $\omega_c(B_{SdH})\tau_{SdH} = 1$ where B_{SdH} is the onset magnetic field, the lowest field where oscillations can be seen. Onsets of $0.075(0.10)T$ for EA137HB(EA100HB) provide values for τ_{SdH} which are about two times larger, namely $5.2(3.9)ps$.

In order to estimate τ_{CR} we follow the same procedure taking into account an extra factor 2 in damping exponential as prescribed by Equation 5.3. The corresponding Dingle plot is shown in Figure 5.8. Here we plot the amplitude of giant CR oscillations in sample EA137HB versus multiplicity index j for two different radiation frequencies. Solid (open) symbols represent the data for microwave frequency of $f = 55GHz$ ($148.5GHz$). Both sets of data show very good agreement with the model, exhibiting clear exponential behavior over two orders of magnitude and extending up to 10-th harmonic for higher frequency. More surprisingly yet, both sets are fitted equally well (solid lines) and reveal the unique value for scattering time $\tau_{CR} = 13ps$. For both frequencies oscillations persist down to the same onset magnetic field B_{CR} of about $250G$ which is approximately

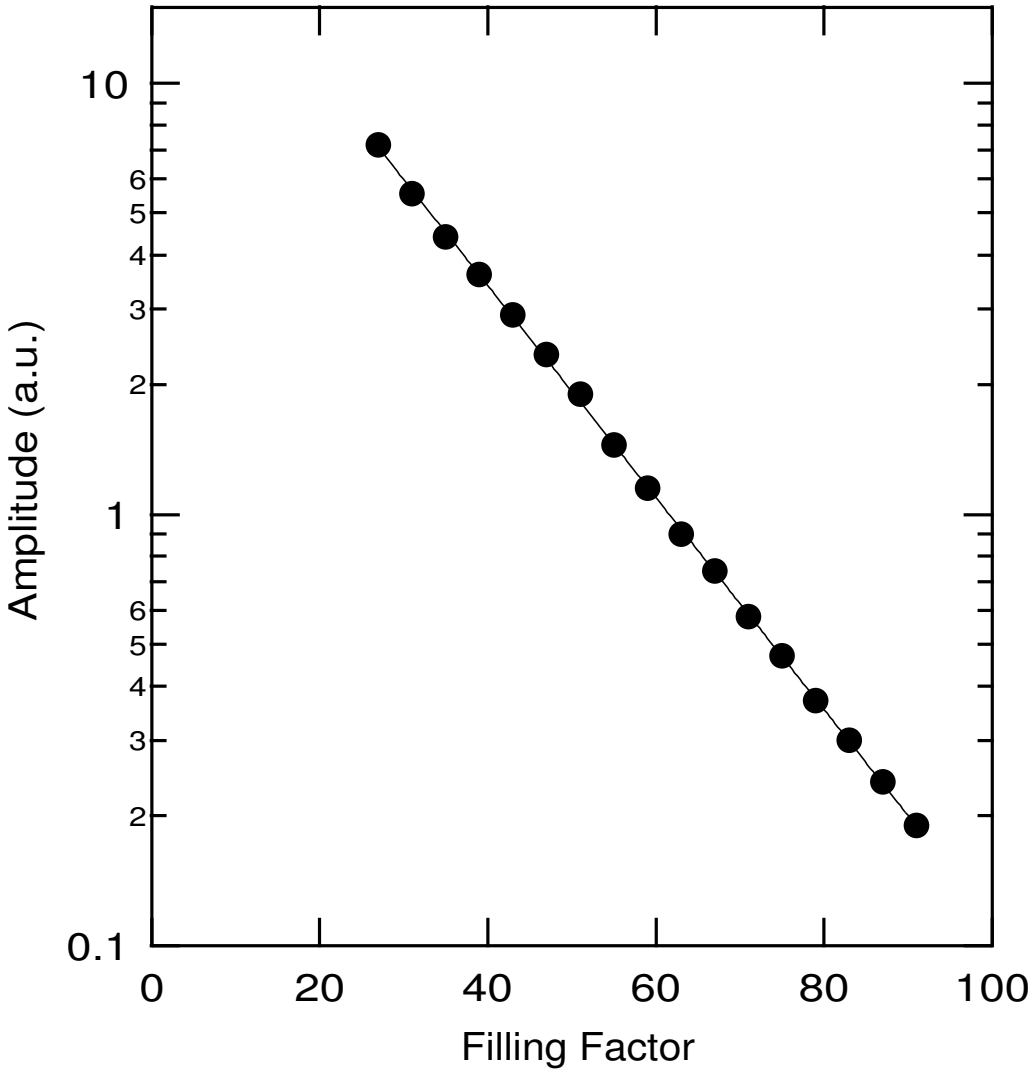

Figure 5.7. Dingle plot for Shubnikov-de-Haas oscillations

three times lower than B_{SdH}. An estimate for scattering time from the condition $\omega_c(B_{CR})\tau_{CR} = 1$ gives slightly higher value of $\sim 16ps$.

Comparing scattering times in these three regimes we speculate that the CR oscillations observed here may not be sensitive to certain properties such as the density inhomogeneity in a 2DES. It is well known [28] that the density inhomogeneity contributes to an underestimate of the experimental value of τ_{SdH}. On the other hand, there is no existing theory dealing with photoconductivity in realistic samples. We also note that a very large CR scattering time, even larger than transport scattering time, has been observed in the extreme quantum limit in a *GaAs-AlGaAs* system [15].

A quantitative fit to the absolute amplitude of the photoresistance oscillations is not attempted since, as has been pointed out in Section 3.4, details of the photoconductive processes remain inadequately understood.

5.5 Fan Diagram for High-Order CR

We have further confirmed our CR results over a wide range of frequency f. In accordance with resonant condition shown in Equation 5.2, the energy required for high-order CR, for a set of *integer* j, is expected to form a fan diagram against the B field position of each resistance maximum. In Figure 5.9, we plot our data for sample EA137VP in just such a diagram covering the whole available range of frequencies f from 30 to $150GHz$.

The open symbols represent the data for each branch $j = 1, 2, 3, 4$, and the dotted lines represent the fans calculated using Equation 5.2 and a value of $0.068m_0$ as the electron mass. Very good agreement between predictions and experimental data is clearly seen over the whole frequency range, further supporting the interpretation of high-order cyclotron resonance.

5.6 Detection of 2D Magnetoplasmon

In addition to the giant amplitude oscillations originating from high-order cyclotron resonance our technique allows to detect another type of low-energy magneto-

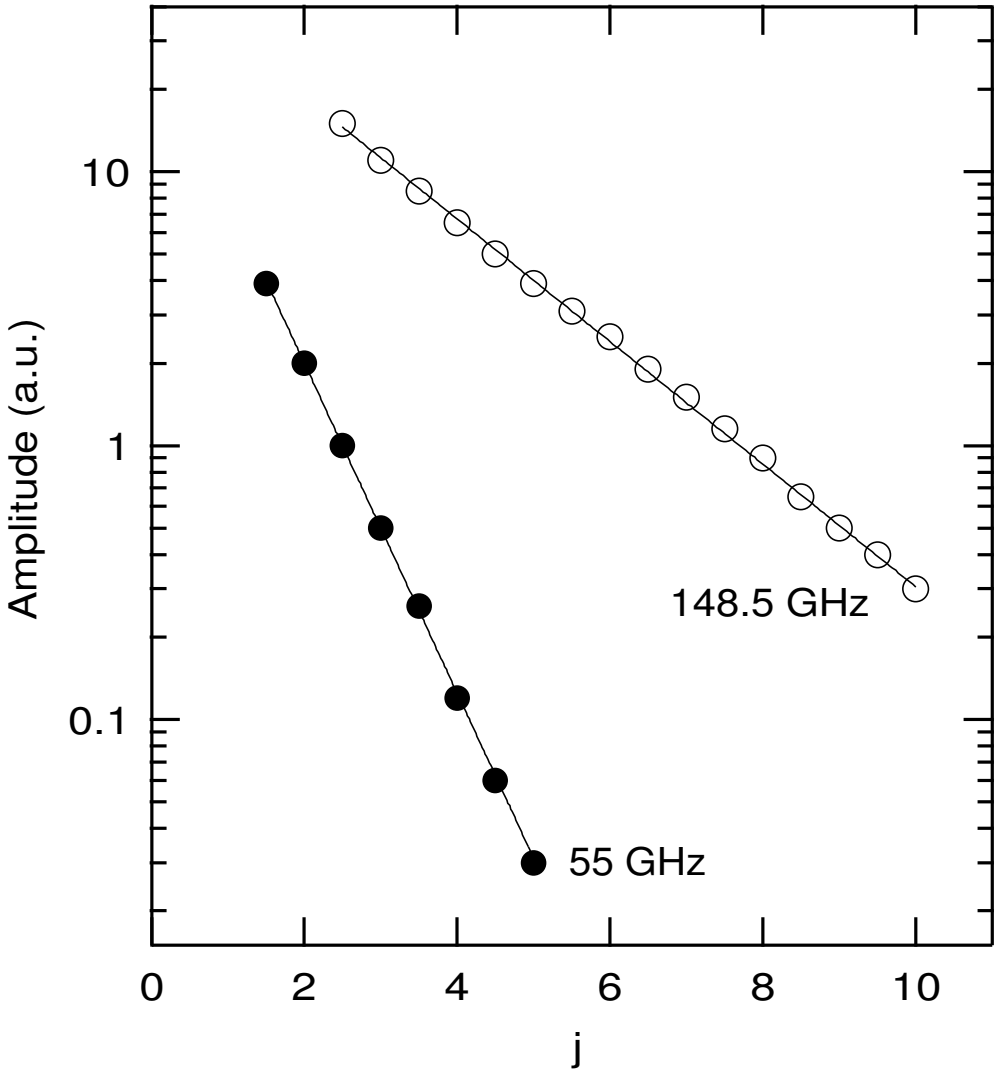

Figure 5.8. Dingle plot for CR oscillations in sample EA137HB for $f = 55GHz$ and $148.5GHz$

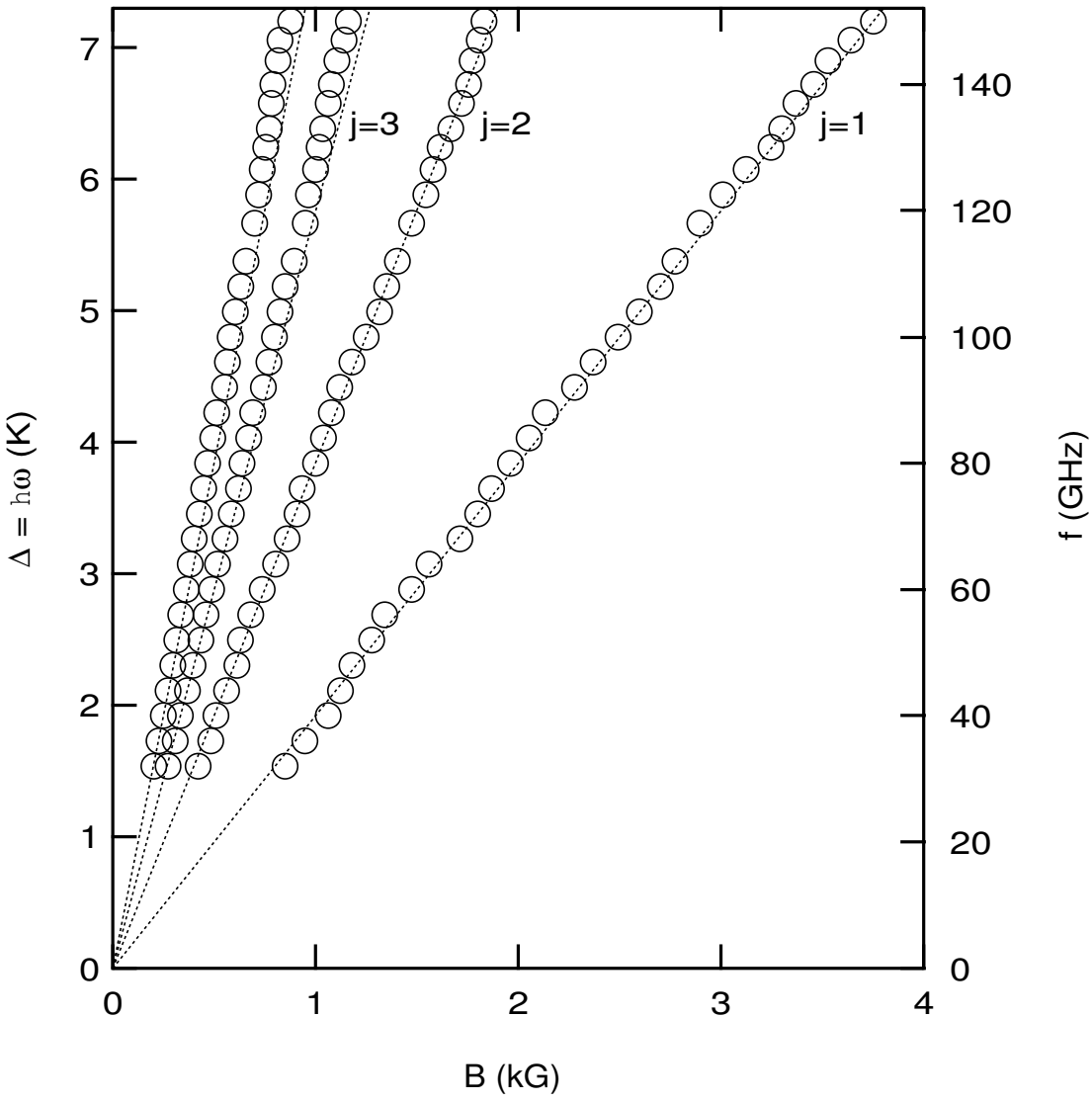

Figure 5.9. Fan diagram for high-order CR in sample EA137VP

excitations, namely, the 2D magnetoplasmon (MP). The dispersion relation in long wavelength limit (Equation 2.29) dictates that the MP can be excited only by coupling to a finite momentum transfer q, usually via a spatially modulated radiation field or electron density [16, 17, 18]. The observation of MP absorption at a specific ω in an un-patterned 2DES implies, then, that a finite q must have been selected in the process. It turns out that what we have observed are just the resonances of the low-frequency MP modes at a cut-off wavelength given by the width of the 2DES sample.

The MPR data for the sample EA100HB ($n = 2.0 \times 10^{11} cm^{-2}$, filled triangles) are shown in fan diagram presented in Figure 5.10. The existence of MPR peaks in our plain 2DES is rather puzzling at first glance. The magnetic field dependence of the resonance energy resembles, when plotted in this fashion, the finite wave vector magnetoplasmon that has been seen [16] in a grating-modulated 2DES at high B fields. However, as dictated by Equation 2.29, it is necessary to introduce a finite q in the 2DES for the MPR to take place. Empirically we fit the MP dispersion (2.29) to our data to find the value of the sample width, using a mass $m^* \approx 0.068 m_0$ and a dielectric constant $\epsilon = 12.9$. Simple fit results in $w \approx 202 \mu m$ which is close to the lithographic width of our Hall bar (see Table 4.1).

It is then convincing that a low-frequency branch of MP is excited by microwave fields in our samples, and detected by the photoresistance measurements. We further note that since polarization of the microwave E field is perpendicular to the Hall bar (see Figure 4.1), the observed MP modes are transverse to the current. They can then be viewed as the standing waves in a 2D waveguide defined by the Hall bar mesa, and these are just the low-frequency cut-off modes. In fact, we have also observed high-order MP modes associated with integer fractions of the sample width.

We also note that for this sample EA100HB the resonant frequency of the fundamental peak $j = 1$ is about 10cyclotron resonance. The origin of this discrepancy is unclear at this point, especially in the light of good agreement obtained for high harmonics. It however may be caused by MP since we have not detected any shift

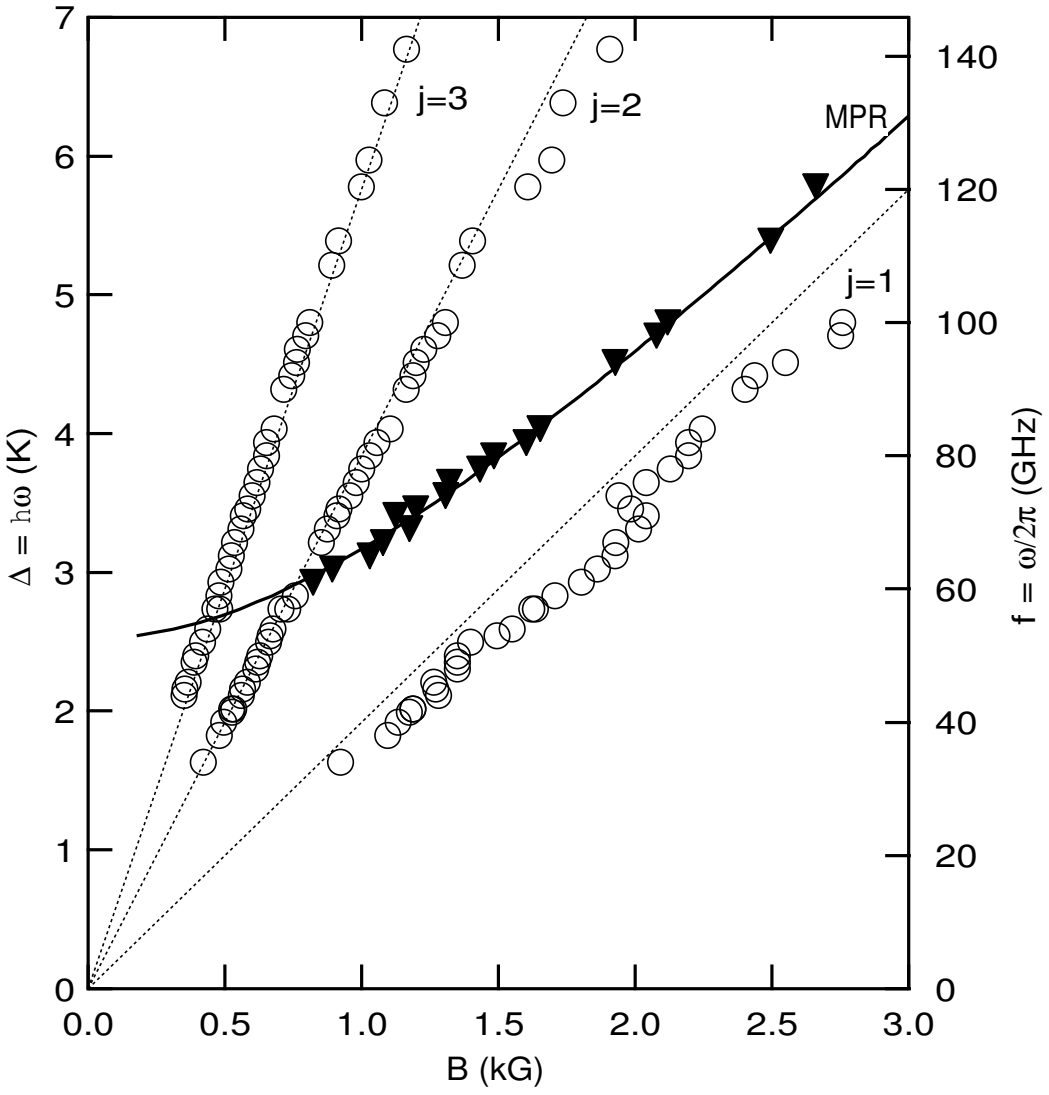

Figure 5.10. Fan diagram for high-order CR in sample EA100HB

in our Van der Paul sample (see Figure 5.9). We also note that this shift disappears at low density/mobility together with high harmonics, as discussed in Section 5.7.

5.7 Cyclotron Resonance at Low Density

Utilizing our variable density sample EA100GT we performed a density dependent study of the high-order CR. Here by varying the gate voltage we were able to tune electron density n from $1.1 \times 10^{11} cm^{-2}$ to $2.5 \times 10^{11} cm^{-2}$. During this experiment the temperature and the millimeterwave frequency were kept constant at $0.4K$ and $57GHz$, respectively. We notice that as the density decreases oscillations become weaker and the fundamental peak gradually shifts toward lower magnetic field. At still lower densities, oscillations disappear completely, and the fundamental CR converges to the theoretically predicted value. In Figure 5.11 we present two photoresistance traces for different densities: a). $n = 2.17 \times 10^{11} cm^{-2}$ and b). $n = 1.12 \times 10^{11} cm^{-2}$. Dashed vertical line are drawn according to the theoretical predictions. It is obvious that oscillations disappear as well as the shift of the fundamental peak. The observed suppression of the high-order CR in lower density is not fully understood but it may be partially accounted for by a decrease in electron mobility as a result of a reduced electron density.

We extend our low-density measurements over a wider frequency range and confirm that neither high harmonics nor magnetoplasma modes are detected in our photoresistance experiment. The fan diagram for this sample is shown in Figure 5.12. Here we include two sets of data for different densities. Open symbols correspond to the data for $n = 2.17 \times 10^{11} cm^{-2}$, while solid symbols represent the data for low electron density of $1.12 \times 10^{11} cm^{-2}$. For the later case we observe good agreement between the measured position of the fundamental peak and theoretical predictions over the whole frequency range.

5.8 Magnetoabsorption Measurements

Having detected high-order CR in photoresistance measurements, a natural question arises on whether high harmonics can be seen in magnetoabsorption.

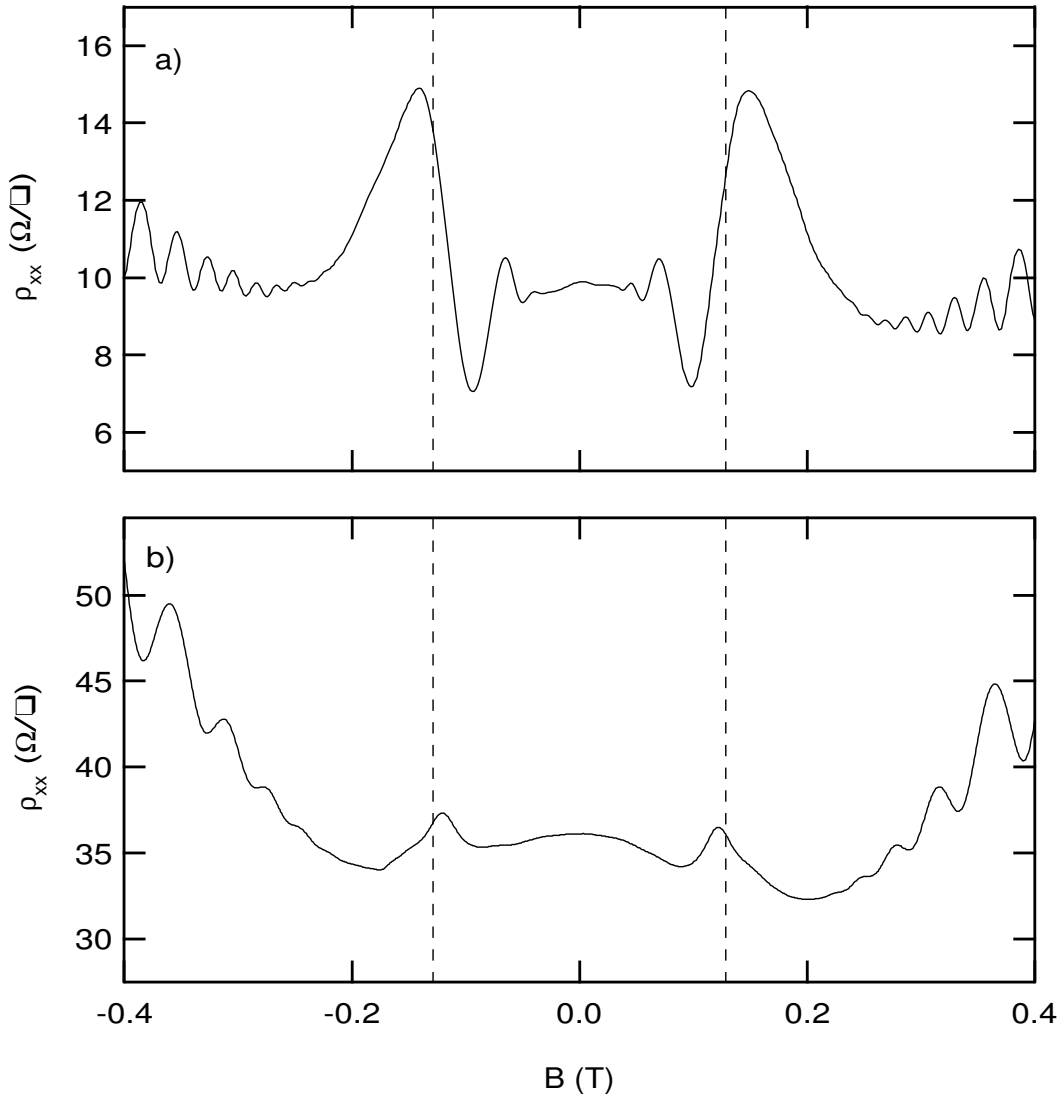

Figure 5.11. CR in sample EA100GT: a). $n = 2.17 \times 10^{11} cm^{-2}$; b). $n = 1.12 \times 10^{11} cm^{-2}$.

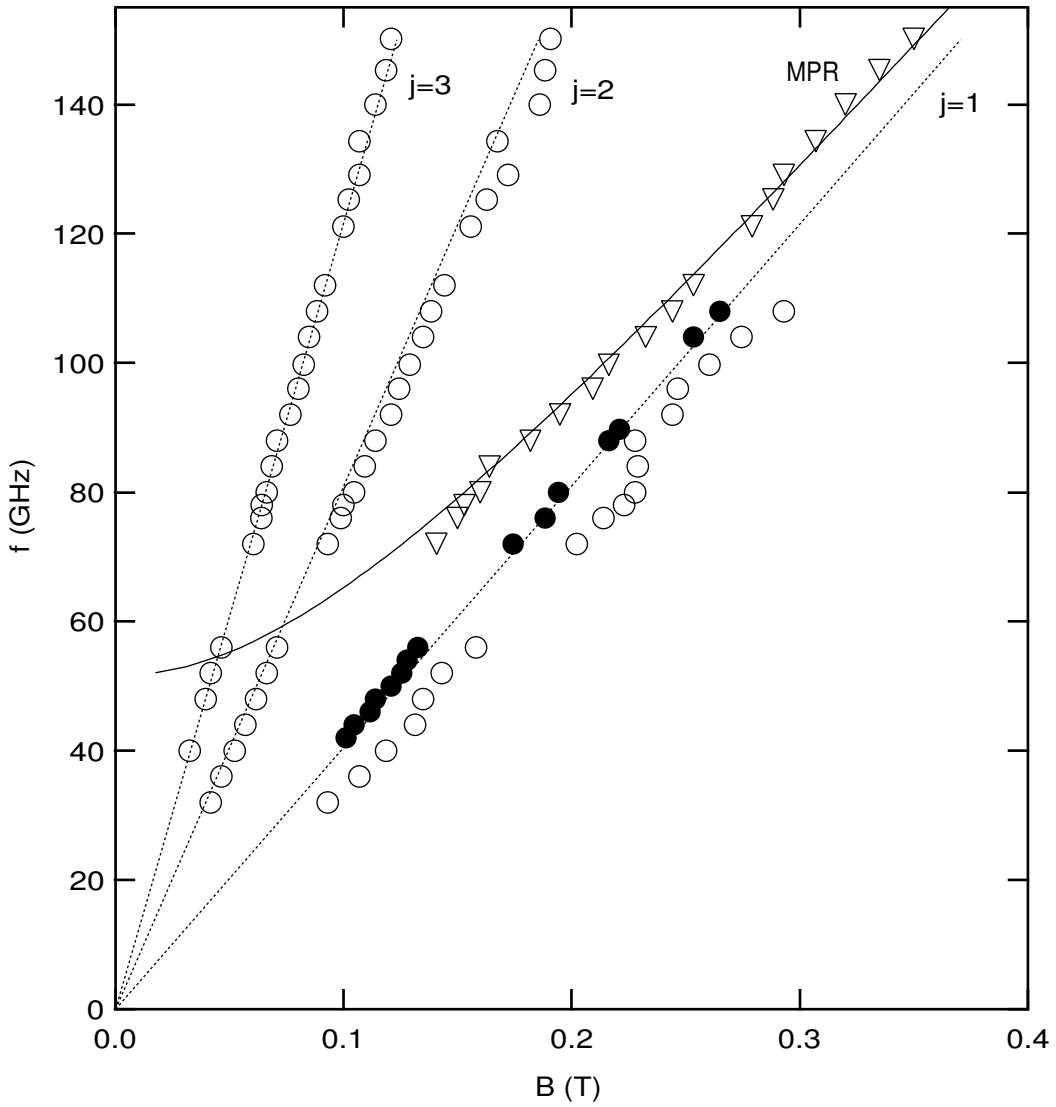

Figure 5.12. Fan diagram for gated sample EA100GT

One can also compare scattering times derived from both approaches. Previous absorption measurements on electron cyclotron resonance revealed rather large scattering time, in some cases even larger than transport scattering time [15]. However the CR scattering time in the low field regime has been largely unknown.

To maximize the bolometer response and at the same time eliminate complications associated with magnetoplasma we have chosen Van der Pauw configuration samples which are large enough to cover the crossection of our WR-28 waveguide. While similar results were obtained both from EA100VP and EA137VP only those from the later will be presented here. Double modulation technique (see Section 4.3) also proved to be more reliable as compared to conventional approach based on DC excitation of the bolometer.

In Figure 5.13 we plot the bolometer response versus applied magnetic field for millimeterwave frequency $f = 145GHz$. Solid line representing the experimental data shows a deep transmission minimum centered at the predicted value of magnetic field. We fit this curve with a theoretical absorption (dotted line) defined by Equation 3.3 to arrive at optical scattering time τ_{CR} of $30ps$. This value is larger

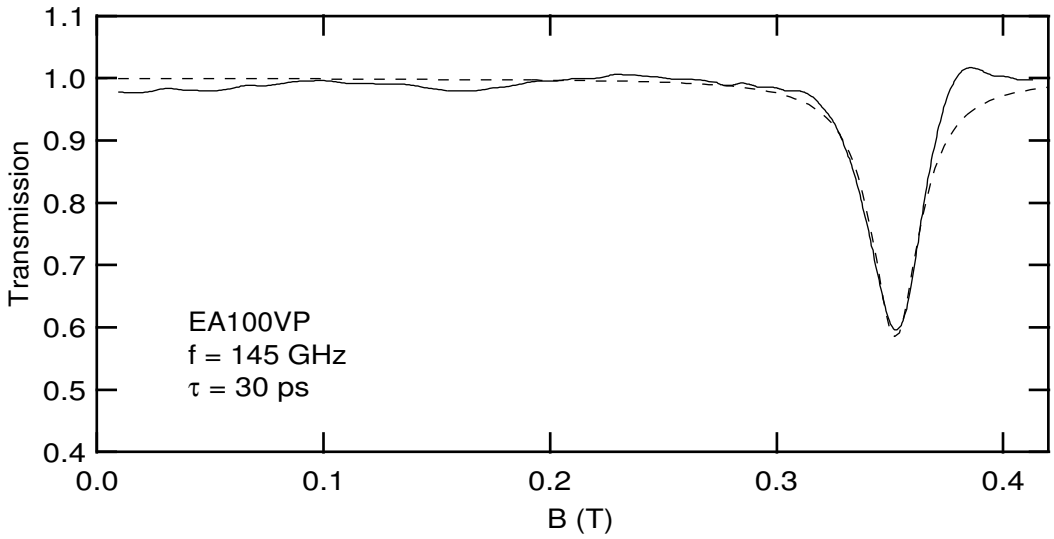

Figure 5.13. Transmittance in EA100VP

than the $\tau_{CR} = 13ps$ extracted from photoresistance. Although the absorption peak is surprisingly strong, there is no signature of high-order CR in the bolometer signal, at least above the noise level.

CHAPTER 6

CONCLUSIONS

To summarize, we have developed a new technique, namely *Millimeterwave Photoconductivity Spectroscopy*, and employed this technique to study low frequency magneto-excitations in 2DES.

Giant oscillations observed in millimeterwave photoresistance in weak magnetic field are identified as originating from high-order CR of electrons. We emphasize that the exceptionally strong high-order harmonic detection observed here is due to the presence of short-range scatterers, ubiquitous in even very clean *GaAs-AlGaAs* heterostructures, and that the presence of high LLs favors large amplitudes for the high-harmonic transitions. The scattering time in this regime appears, however, about five times larger than that determined by the Dingle plot in the SdH regime. This observation may be attributed to the different roles played by density inhomogeneity in these two regimes. We have also identified distinct resonances of the low-frequency magnetoplasmon modes at a cut-off wavelength, determined by the width of the sample. This work thus establishes a method for the detection of low-energy magneto-excitations close to the Fermi surface of a 2DES.

Since microwave photoresistance technique has been proven to be very powerful in low-field limit, we discuss the possible implication of this technique to the measurements around filling factor $\nu = 1/2$.

In low magnetic field B or high electron filling factor ν the system behaves as a 2D electron metal. Due to the existence of the Fermi energy ε_F and cyclotron energy $\hbar\omega_c$ SdH oscillations arise. In our experiment we have shown that if one introduces a new energy scale this system can also exhibit giant oscillations due to high-order CR.

According to CF theory [5, 6] interacting electron system around half-filling can be viewed as a system of weakly interacting CF in low effective magnetic field. This 2D CF metal also exhibits SdH effect and therefore one can try to apply microwave photoresistance technique to look for resonant response of CFs which would provide a direct probe for CF effective mass, presently known only from the DC magnetotransport experiments.

As described in Section 2.6 the energetics of CF system is entirely determined by electron-electron interactions. A fundamental theorem, Kohn's theorem, states that long wavelength electro-magnetic radiation only affects the center-of-mass motion and does not couple to the correlations in a homogeneous system. It is then necessary to introduce a finite q to probe the interaction effects. This is traditionally accomplished by placing a metal surface grating in the vicinity of the 2DEG. Such a grating may be fabricated by high-resolution e-beam lithography and lift-off techniques. Finite wave vector q needed for study correlation effects is defined as $q = 2\pi/nd$, where d is the periodicity of the grating, and n is an integer.

Besides the fundamental difficulties of coupling the radiation fields to electron-electron interactions, we discuss possible limitations imposed by the CF scattering time. From transport measurements in high magnetic fields it is known that the corresponding energy scale is about $40GHz/T$ (see Table 3.1) which corresponds to millimeterwave frequency range. Another important issue is the sample quality needed for the detection of the CF resonance. First of all, in low B field giant oscillations have been detected in the high ν limit, namely $30 < \nu < 300$ where the effect may be enhanced due to strong mixing of multiple LLs. SdH effect is seen up to $\nu \approx 100$ in our samples. If one takes this sample to high magnetic field we observe that SdH effect of CFs persists only up to the filling factor $p \approx 6$. In addition to that, the Fermi energy of CFs $\varepsilon_F^{CF} \sim 16K$ is about five times smaller as compared to electron case which decreases the maximum temperature of the experiment. If one estimates CF scattering time τ_t^{CF} from the resistivity at zero effective field ($\nu = 1/2$) it turns out to be about $5ps$ in our samples, which is at least 20 times smaller as compared to electron scattering time τ_t. From

the photoresistance studies in low magnetic field we know that CR can not be detected in low mobility ($\sim 10^6 cm^2/Vsec$) samples. This would set the cut-off scattering time to be about $40ps$ which exceeds well the value of $5ps$ in the present sample. We note, however, that similar oversimplified comparison of electron and CF scattering times predicts no geometric resonance for CFs which, in fact, was detected experimentally [8].

Based on extremely high sensitivity of microwave photoresistance in low magnetic field and successful detection of low energy magnetoexcitations we believe that the developed technique should be further exploited to study interaction effects in high magnetic field. Established finite q studies so far include light scattering [38] and surface acoustic wave [11] experiments. Being very powerful these studies, however, so far have provided only an *indirect* method to measure the CF effective mass. Moreover the frequency dependence of the response function of the CF system has not been studied at all. We hope that our approach, which combines finite q and ω, may open a new experimental window in studies of correlation physics in 2DES.

APPENDIX A

DIFFERENTIAL PHOTOCONDUCTIVITY TECHNIQUE

Now let us demonstrate the techniques discussed above on a sample data trace. In this case we illuminate the sample EA137 with millimiterwave radiation of frequency $f = 55GHz$. Sample is kept at temperature of about $2K$. Although the units in all figures are arbitrary, they allow the quantitative comparison among the traces.

Trace in Figure A.1 shows the longitudinal resistance of the sample illuminated by a continuous beam of radiation. Giant oscillations are clearly seen here although being superimposed on the background of negative magnetoresistance and somewhat smeared by SdH oscillations.

An attempt to use the simplest realization of differential photoconductivity described by Equations 4.5 results in a trace shown in Figure A.2 which reveals strong contamination of the photoresistance with photovoltage signal and thus gives no improvement over previous trace.

Employing the double modulation technique results in virtual separation of the signals $I_{ex}\Delta R$ and $I_{ph}\left(R + \Delta R\right)$ which are shown in Figure A.3 and Figure A.4 respectively. The photoresistance trace is a replica of the trace in Figure A.1 with the background subtracted. In general, weak periodic structure in SdH regime appears as a consequence of temperature dependence of SdH oscillations thus reflecting the heating due to radiation. In this particular case of higher temperature this effect can be suppressed given the fact that the radiation power is not too strong. This further improves the trace eliminating SdH oscillations from the consideration which is particularly important at higher radiation frequencies. It

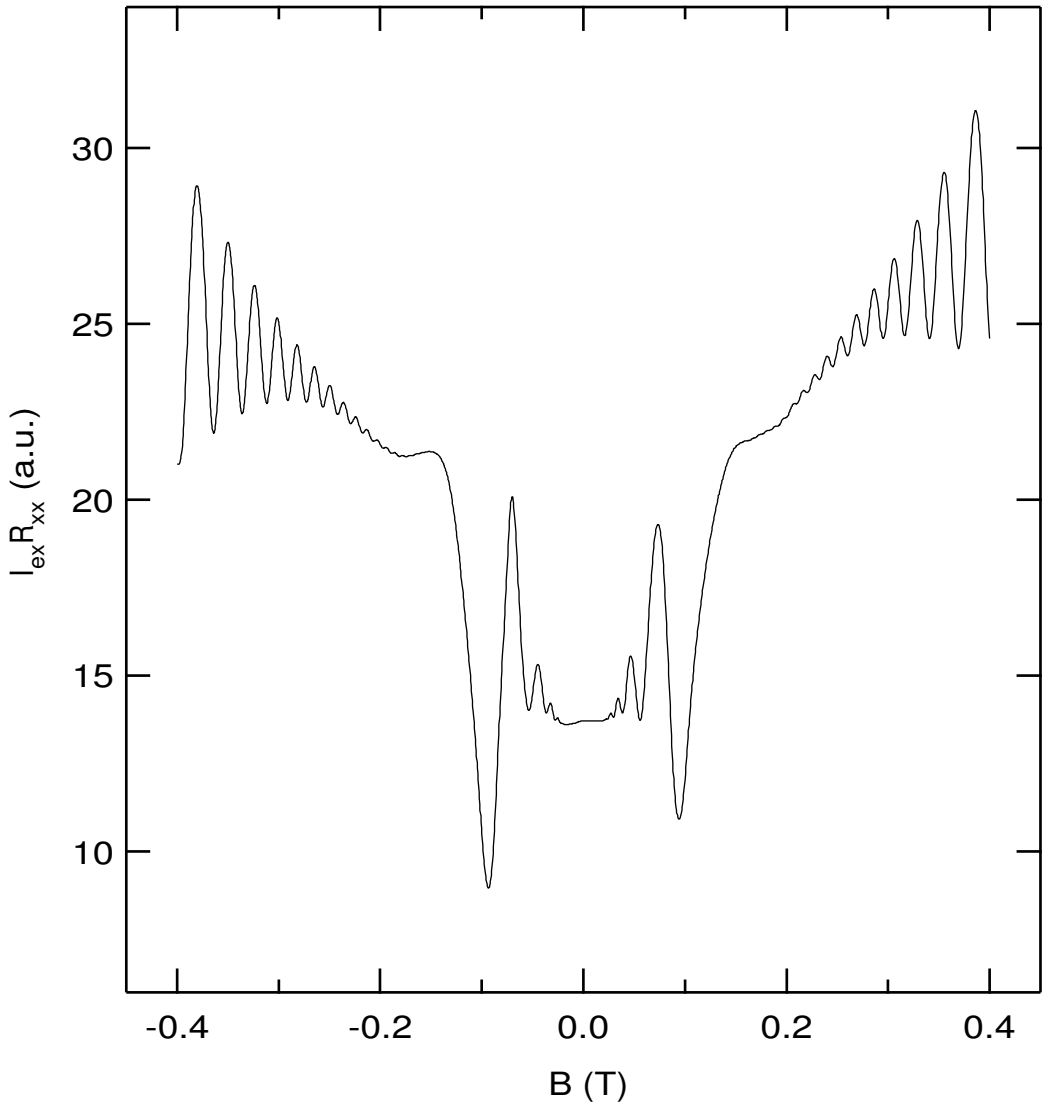

Figure A.1. Resistance under continuous illumination

is obvious that the resolution is greatly enhanced in this case since the trace clearly shows the alternating sign of the photoresistance and reveals more harmonics as compared to one in Figure A.1.

The shape of the photovoltage trace in in Figure A.4 is rather complicated for analysis. It demonstrates (together with Figure A.2), however, that separation

is absolutely necessary since photovoltage magnitude exceeds the photoresistance signal, in some cases by two orders of magnitude.

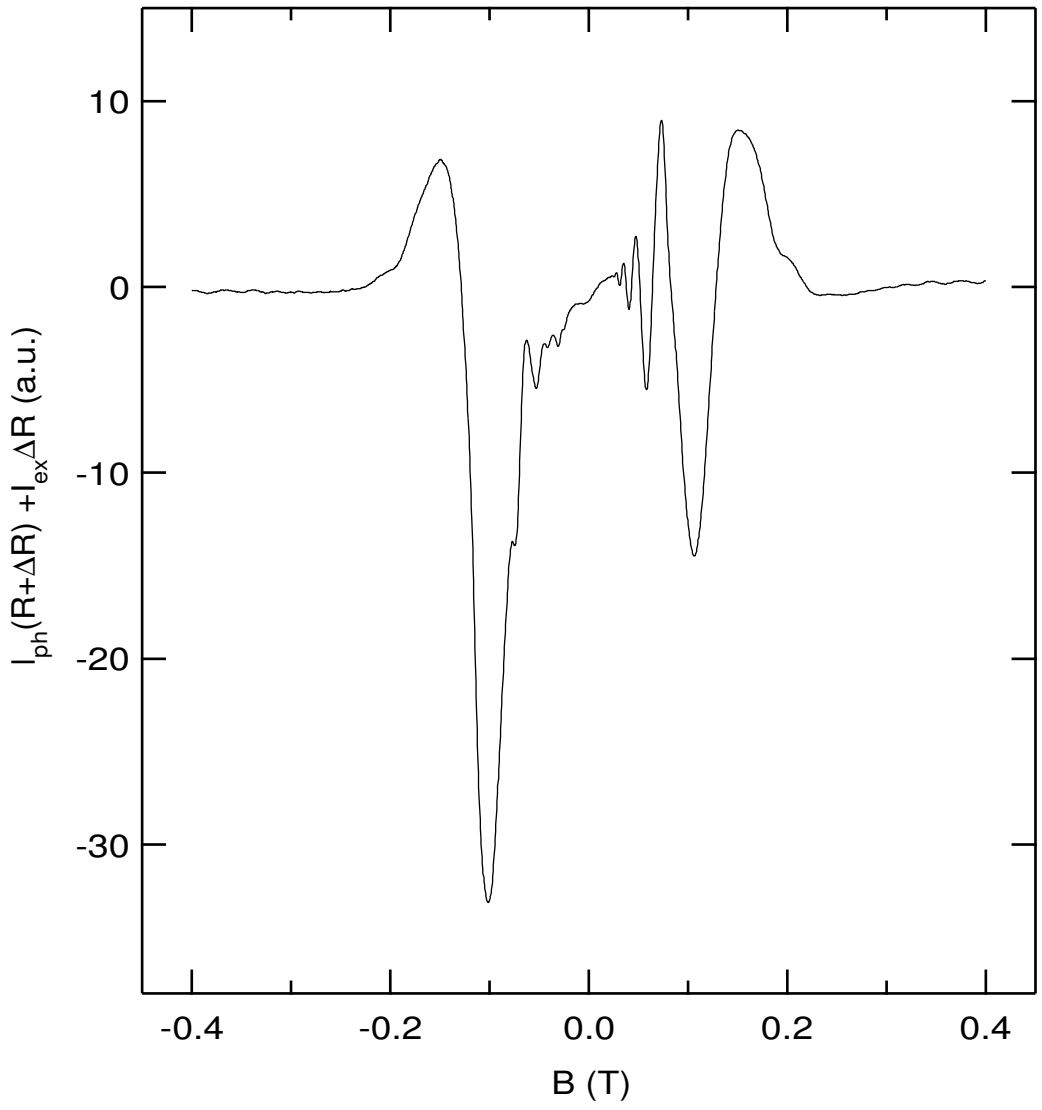

Figure A.2. Photoresistance with single modulation

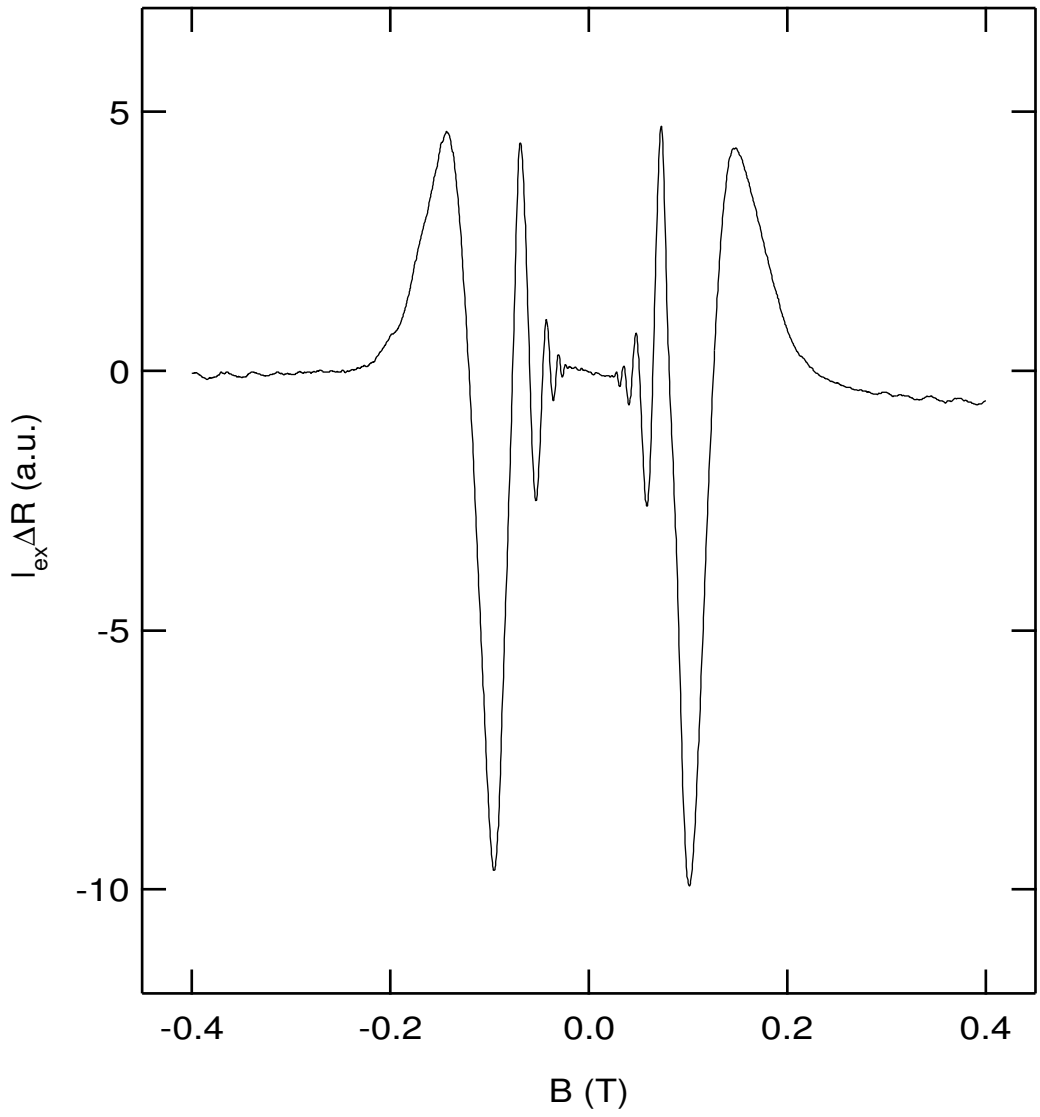

Figure A.3. Photoresistance with double modulation

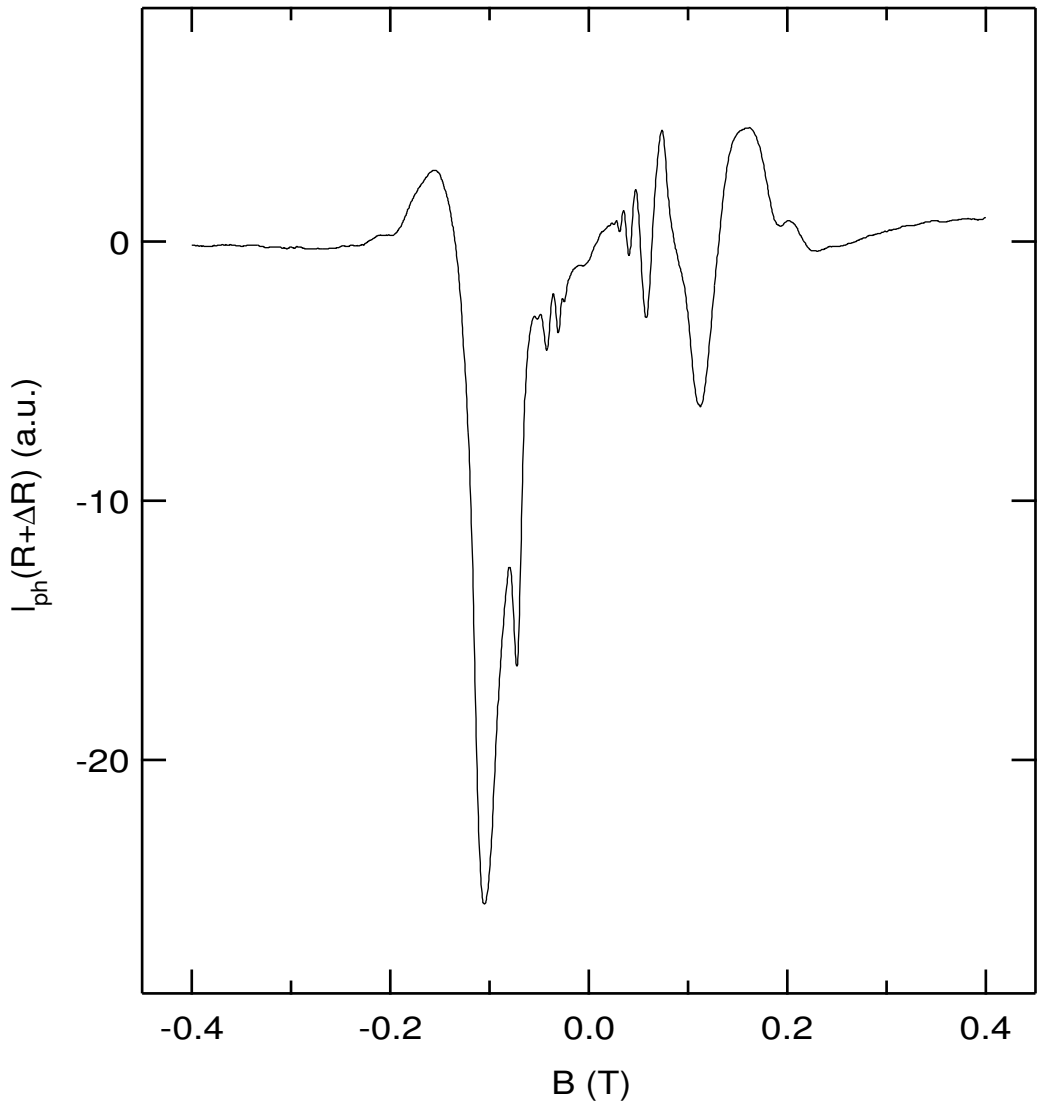

Figure A.4. Photovoltage with double modulation

APPENDIX B

APPARENT RESONANCE STRUCTURE IN WEAK FIELD MAGNETORESISTANCE IN A PLAIN 2DES

It is well known that in a plain 2DES Shubnikov-de Haas effect dominates the magnetoresistance $R_{xx}(B)$ in a weak B field. We have, however, observed sharp $R_{xx}(B)$ structure beyond SdH (in the $B < 0.3T$) in our high mobility 2DES. The observed $R_{xx}(B)$ structure is roughly periodic in $1/B$, and resembles that of geometric resonance in a strong 2D periodic potential. In the following we summarize the experimental data and discuss the relative merits of two possible interpretations of the phenomenon, namely the magneto-acoustic phonon resonance (MAPR) and the geometric resonance (GR).

B.1 Experimental Data

While similar features have been observed in a variety of samples, here, we limit our discussion to the data taken from two samples, the EA100HB and a variable density sample EA100GT where the electron density can be controlled via $NiCr$ gate. The mean free path l estimated from the DC mobility is about $20\mu m$.

In Figure B.1 we show typical trace of magnetoresistivity in sample EA100HB $\rho_{xx}(B)$ at ^4He temperature. At this temperature Shubnikov-de Haas (SdH) oscillations are rather weak. Our data show another series of magnetoresistance oscillations which appear at low magnetic field ($B < 0.3T$) and form a structure which is roughly periodic in $1/B$.

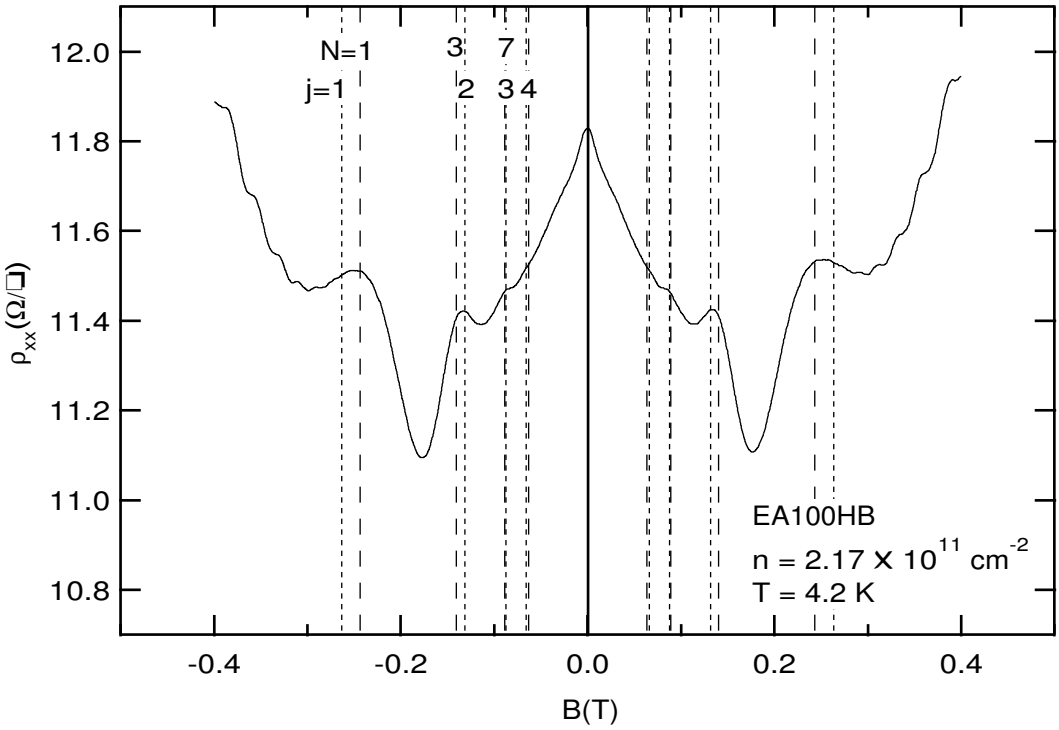

Figure B.1. Magnetoresistance oscillations beyond SdH effect

One can also increase the resolution by removing the background due to strong magnetoresistance. Taking the second derivative of the magnetoresistance presented in Figure B.2 allows to reveal high-order GR modes. Here we plot the data from sample EA100GT with an electron density $n = 2.52 \times 10^{11} cm^{-2}$.

The next step was to see how the observed oscillations depend on temperature. In Figure B.3 we present magnetoresistivity traces taken at several temperatures from 1.9 to $10.5K$. Vertical dashed lines indicate the positions of the maxima of oscillatory structure.

We observe that oscillations are best developed in a very narrow temperature window around $5K$. As the temperature temperature deviates from this value oscillations are strongly damped and are barely seen both at lower $\sim 2K$ and higher $\sim 8K$ temperatures. We also notice that negative magnetoresistance seen at lower T is replaced by positive at higher T, with the transition point again at about $5K$. Another set of data for sample EA100GT at density $n = 2.04 \times 10^{11} cm^{-2}$ presented in Figure B.4 shows similar behavior.

The structure presented in Figure B.1 may, in principle, arise from SdH effect of electrons occupying the second subband of potential well. however, in *GaAs-AlGaAs* heterostructure the value of intersubband separation is typically $> 200K$ while the Fermi energy E_F in our sample is about $80K$ (see Table 3.1). Therefore, as discusssed in Section 2.1 one can not expect considerable population of the second subband at low temperature. In addition, corresponding Landau splitting ($\hbar eB/m^*$) is less than $2K$ in this magnetic field range and therefore it is unlikely to observe SdH effect at $4K$. Finally, the fact that the oscillations are strongly suppressed at lower temperature (see, *e.g.*, Figure B.3) is inconsistent with SdH. Therefore, we conclude that SdH effect from the second subband can not account for the observed oscillatory structure.

B.2 Magneto-Acoustic Phonon Resonance

One possible explanation is based upon the picture of magneto acoustic phonon resonance (MAPR). Using the temperature dependent data in Figure B.3 we construct Figure B.5 which shows the inverse DC mobility versus temperature.

Linear behavior indicates that acoustic phonon scattering dominates the electron mobility [39, 40, 41] in this temperature range. The lowest temperature T_{ph} for this linear behavior can be estimated from the energy of acoustic phonon with the wave vector which is just twice the Fermi wave vector $q = 2k_F$ [41]

$$T_{ph} = \frac{\hbar u_s(2k_F)}{k_B} \tag{B.1}$$

Here u_s is sound velocity in $GaAs$ (see Table 2.1) and k_B is Boltzmann constant. Calculations applied to our sample yield $T_{ph} \simeq 5.1K(107GHz)$. We note, that this is the temperature where the oscillations are best observed. At lower temperatures only phonons with small wave vectors can participate in scattering and therefore there may be no backscattering. Therefore, it is natural to think that oscillations may be related to acoustic-phonon scattering.

Strong backscattering is the process of electron excitation across the Fermi surface. The $2k_F$ change in electron momentum is accommodated by acoustic phonon; however, at zero magnetic field there is a problem with the energy conservation. In finite magnetic field, an extra energy caring by $2k_F$ phonon can be absorbed by an electron undergoing a transition between LLs separated by cyclotron gap. However, the selection rule corresponding to $2k_F$ scattering is known to break down in finite magnetic field. If one, however, assumes that the selection rule corresponding to strong back-scattering still holds in finite magnetic field one can try to analyze the oscillations in terms of magneto acoustic phonon resonance. We immediately notice that the Landau splitting at the first oscillation is roughly the same as phonon energy E_{ph} with $q = 2k_F$. If one now treats the effect as a phonon-induced high-order cyclotron resonance one should write the resonant condition by analogy with Equation 5.2

$$E_{ph} = 2\hbar u_s k_F = j \cdot \hbar\omega_c \tag{B.2}$$

where j is an *integer*. From this equation we calculate the positions for high-order resonances up to $j = 4$ which are represented in Figure B.1 by dotted lines. We note that even better agreement is achieved for high harmonics. There is no adjustable parameters in this treatment, only the assumption about strong back scattering in finite magnetic field. The lack of selection rule is responsible for the fact that MAPR has never been observed. Observation of MAPR requires a fundamental mechanism to recover the $B = 0$ selection rule and therefore is very interesting.

B.3 Geometric Resonance

Geometric resonance (GR) in 2DEG has been extensively studied during the recent past [42, 43]. The effect arises from introducing a new length scale into a system via periodic 1D (or 2D) potential (or density) modulation. In a weak magnetic field, commensurability of a cyclotron radius R_c with a modulation period d results in a series of magnetoresistance oscillations roughly periodic in inverse magnetic field. More relevant to the following discussions, a strong 2D potential modulation is usually realized via etching a periodic lattice of microscopic holes into high-mobility 2DEG, commonly known as anti-dot superlattice. The main transport features, then, can be explained classically [42, 43] given the fact that electron mean free path $l = \hbar k_F \mu / e$ is much greater than d. In this picture, when classical electron encircles a certain number of anti-dots it becomes essentially localized thus causing an increase in resistivity. This situation occurs at selected values of magnetic field determined by the ratio of the lattice period d to the cyclotron radius R_c given by

$$R_c = \frac{\hbar k_F}{eB} \tag{B.3}$$

and therefore magnetoresistance oscillations arise. It is obvious, then, that in-

tentional modulation has to be introduced in 2DEG before GR can take place. However, the observed weak-field ($B < 0.3T$) oscillations are reminiscent to GR in several ways.

It is known that simple geometrical analysis of classical orbits can yield the information about symmetry (*i.e., triangular* or *square* lattice), period d, and the anti-dot radius r. Our results seem to be consistent with a triangular lattice, while square and 1D modulation potentials can not account for the observations.

In a triangular lattice one can divide all possible pinned orbits into three groups *(I, II, III)* with the lowest mode encircling 1, 2 or 3 antidots respectively. Simple geometrical analysis leads to the following pinned orbits, number indicating the number (N) of surrounded anti-dots:

$$\begin{array}{lllllllll} I: & 1, & 7, & 13, & 19, & 31, & ... & & \\ II: & 2, & 4, & 8, & 10, & 14, & 18, & 22, & ... \\ III: & 3, & 6, & 12, & 18, & 21, & ... & & \end{array}$$

For each N there is a range of possible pinned orbits contained within a ring $R^N_{max} - r < R_c < R^N_{min} + r$, where r is the radius of anti-dot and R^N_{max} (R^N_{min}) is maximum(minimum) allowed R_c for $r = 0$. The width of the ring ΔR^N_c is defined as follows:

$$\Delta R^N_c = (R^N_{max} - r) - (R^N_{min} + r) \tag{B.4}$$

In our simple analysis we assume that the peak in resistance for mode N occurs when electron orbit lies in the center of the ring R^N_c, *i.e.*

$$R^N_c = \frac{(R^N_{max} - r) + (R^N_{min} + r)}{2} = \frac{R^N_{max} + R^N_{min}}{2} \tag{B.5}$$

which is independent on r.

Since R^N_{max} and R^N_{min} can be easily expressed in terms of the lattice period d, given the symmetry of the lattice, we obtain the whole spectrum of R^N_c and ΔR^N_c which are presented in Table B.1.

To compare the model with experiment it is convenient to formulate the GR resonant condition in terms of magnetic fields. Using Equation B.3 we conclude that the maxima in resistance occur at magnetic fields proportional to Fermi wave-vector k_F:

$$B^N = \frac{\hbar k_F}{eR^N_c} \tag{B.6}$$

Then, fitting the first maximum in the data to the B^1 yields $d = 0.62\mu m$. Using this value we calculate magnetic field positions B^N for other pinned orbits R^N_c, which are also presented in Table B.1. Comparing the corresponding B^N field positions with experimental trace in Figure B.1 we find that peaks in resistance are well described by GR condition (B.6) for $N = 1, 3, 7, 12$. These GR modes are marked by vertical dashed lines in Figures B.1 and B.2.

In order to understand qualitatively why only these modes are detected it is necessary to take into account the radius of the anti-dots. The geometrical width of the ring ΔR^N_c (see Equation B.4) can be related to the certain magnetic field range ΔB^N via the following expression

$$\Delta B^N = \frac{\hbar k_F}{e}\left[\frac{1}{R^N_{min} + r} - \frac{1}{R^N_{max} - r}\right] \tag{B.7}$$

It is clear that with increasing r/d fewer modes are to be observed since rings tend to collapse. Calculations for ΔB^N presented in Table B.1 indicate that for $r = 0.1d$ one can expect to see almost all of the lowest modes. If, however, $r = 0.2d$, then only $N = 1, 3$ and 7 survive. This implies that in our case r is somewhat between $0.1d$ and $0.2d$. Intuitively, one can also expect that the width of the ring ΔR^N_c can be related to the strength of mode N.

Table B.1. GR modes in triangular anti-dot superlattice with period $d = 0.62\mu m$

N(I)	1	7	13	19
$R^N_{\min}(d)$	0	$\sqrt{1}$	$\sqrt{3}$	$\sqrt{4}$
$R^N_{\max}(d)$	$\sqrt{1}$	$\sqrt{3}$	$\sqrt{4}$	$\sqrt{7}$
$R^N_c(d)$	0.5000	1.3660	1.8660	2.3229
$B^N(T)$ $(n = 2.17 \times 10^{11} cm^2)$	0.2440	0.0893	0.0654	0.0525
$\Delta B^N(T)$ $(r = 0.1d)$	1.0844	0.0362	0.0024	0.0102
$\Delta B^N(T)$ $(r = 0.2d)$	0.4575	0.0220	–	0.0056

N(II)	2	4	8	10
$R^N_{\min}(d)$	$\sqrt{\frac{1}{4}}$	$\sqrt{\frac{3}{4}}$	$\sqrt{\frac{7}{4}}$	$\sqrt{\frac{9}{4}}$
$R^N_{\max}(d)$	$\sqrt{\frac{3}{4}}$	$\sqrt{\frac{7}{4}}$	$\sqrt{\frac{9}{4}}$	$\sqrt{\frac{13}{4}}$
$R^N_c(d)$	0.6830	1.0945	1.4114	1.6514
$B^N(T)$ $(n = 2.17 \times 10^{11} cm^2)$	0.1786	0.1115	0.0864	0.0739
$\Delta B^N(T)$ $(r = 0.1d)$	0.0441	0.0265	–	0.0046
$\Delta B^N(T)$ $(r = 0.2d)$	–	0.0058	–	–

N(III)	3	6	12	18
$R^N_{\min}(d)$	$\sqrt{\frac{1}{3}}$	$\sqrt{\frac{4}{3}}$	$\sqrt{\frac{7}{3}}$	$\sqrt{\frac{13}{3}}$
$R^N_{\max}(d)$	$\sqrt{\frac{4}{3}}$	$\sqrt{\frac{7}{3}}$	$\sqrt{\frac{13}{3}}$	$\sqrt{\frac{16}{3}}$
$R^N_c(d)$	0.8660	1.3411	1.8046	2.1955
$B^N(T)$ $(n = 2.17 \times 10^{11} cm^2)$	0.1409	0.0910	0.0676	0.0556
$\Delta B^N(T)$ $(r = 0.1d)$	0.0644	0.0118	0.0134	0.0007
$\Delta B^N(T)$ $(r = 0.2d)$	0.0292	–	0.0058	–

Alternative way to estimate r is from the condition of quenching of the lowest mode at some magnetic field B_q corresponding to situation when the cyclotron orbit R_c^1 can fit between two adjacent anti-dots, namely $2R_c^1 = d - 2r$. From the trace we estimate B_q to be about $0.3T$ yielding $r = 0.13d$, which is consistent with the number of observed GR oscillations.

The observed temperature dependence, however, contradicts to what is known about regular GR. The critical temperature T_c at which the GR disappears may be estimated from the condition where the smearing of the cyclotron orbit due to temperature ΔR_c^T becomes roughly equal to the lattice period d:

$$k_B T_c \simeq \hbar \omega_c k_F d/2 \tag{B.8}$$

T_c calculated from Equation B.8 is about $180K$ which is much higher than observed $8K$. Even more puzzling is the disappearance of oscillations at lower T. We also mention that very weak temperature of GR oscillations is well established experimentally up to $50K$.

Absence of the intentional periodic potential modulation already indicates that what we have observed is not ordinary GR. Extracted value of the lattice period d of $0.62\mu m$ can not be related to any intrinsic length scale in the system. In addition, peculiar temperature dependence contradicts to that known in modulated systems.

B.4 Discussion

Both possible mechanisms imply similar density dependence of the peak positions since both the phonon energy(MAPR) and cyclotron radius (GR) are proportional to $k_F = \sqrt{2\pi n}$.

Utilizing our variable density sample EA100GT we performed a series of measurements at different densities covering the range from 1.5 to $2.5 \times 10^{11} cm^{-2}$. In Figure B.6 we present the quadratic plot showing the dependence of magnetic field for the lowest ($N = 1/j = 1$) mode on the Fermi wave vector. From the slope in Figure B.6 we can estimate the sound velocity in $GaAs$ $u_l = 2.7km/s$ which

compares well with the known value (see Table 2.1) used to generate vertical lines in Figure B.1. On the other hand the slope can be related to lattice period d using Equation B.7 for $N = 1$ yielding $0.63\mu m$, close to already established value of $0.62\mu m$.

The manifestation of GR and the MAPR in magnetoresistance can be quite similar because both of them exhibit 1) periodical oscillations in $1/B$, and 2) positions of the maxima $\propto k_F = \sqrt{2\pi n}$.

In summary, we have observed new, weak field magnetoresistance oscillations in high mobility 2DEG. Such effect can not be explained by a simple mechanism based on SdH effect of electrons in a second subband. Both GR and MAPR which resemble such effect has been examined and their relative merits discussed. Further experiments with a wider range of high mobility, and higher density up to $(4 \times 10^{11} cm^{-2})$ samples may help to clarify the issue.

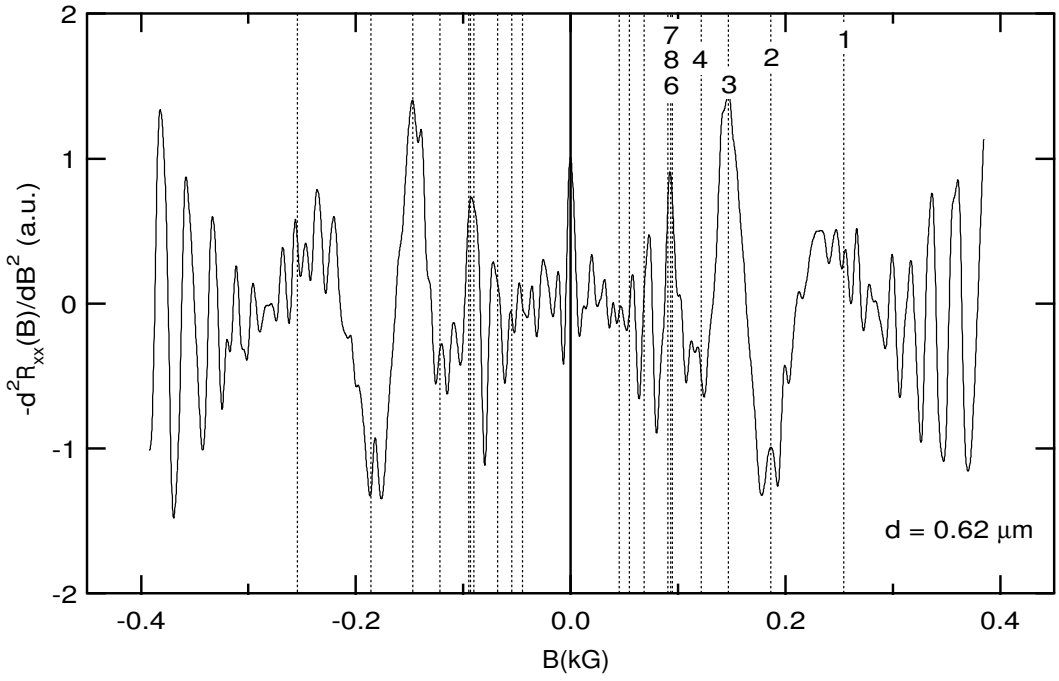

Figure B.2. Magnetoresistance oscillations seen in second derivative

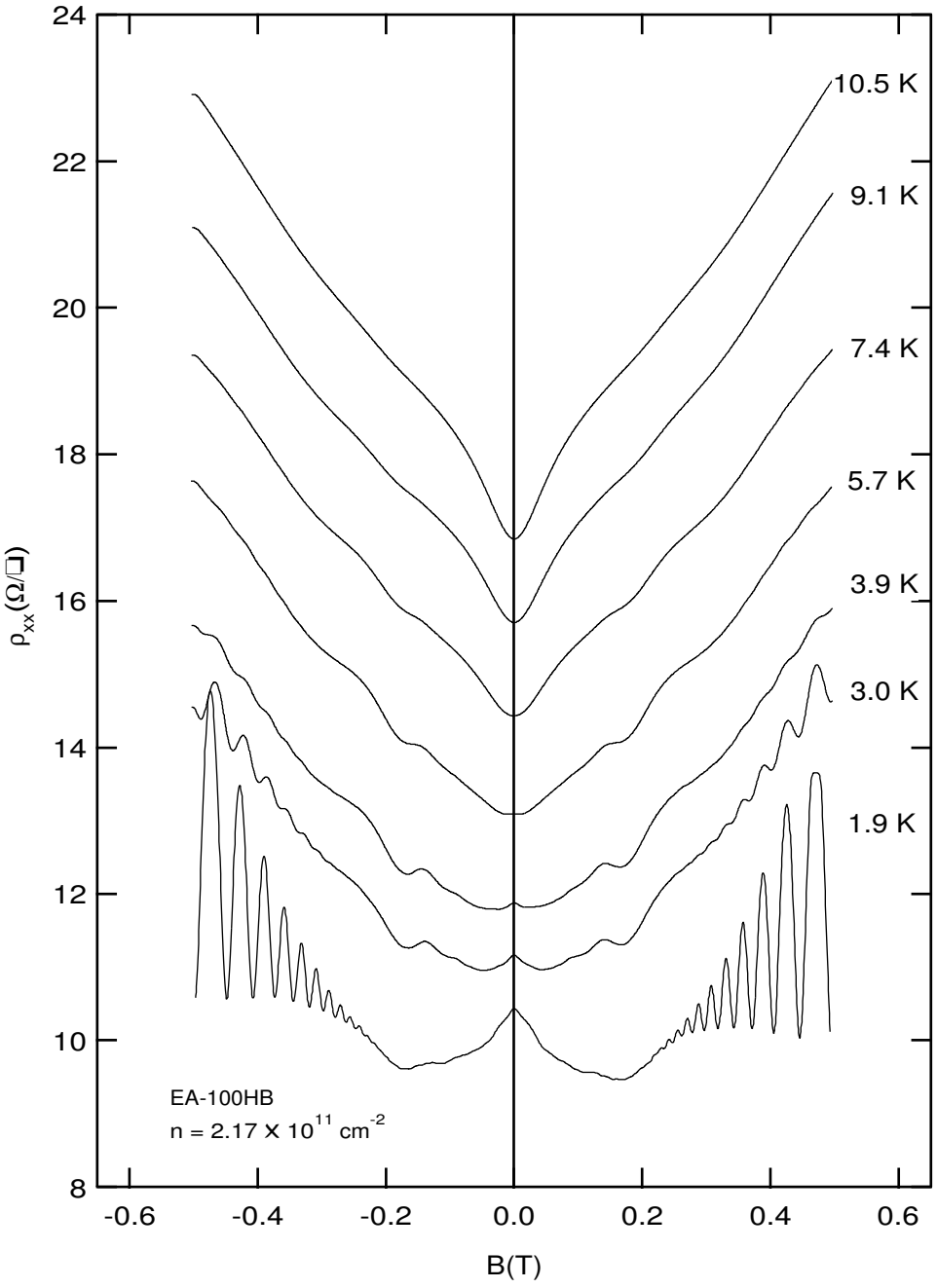

Figure B.3. Temperature dependence of magnetoresistance oscillations in EA100HB

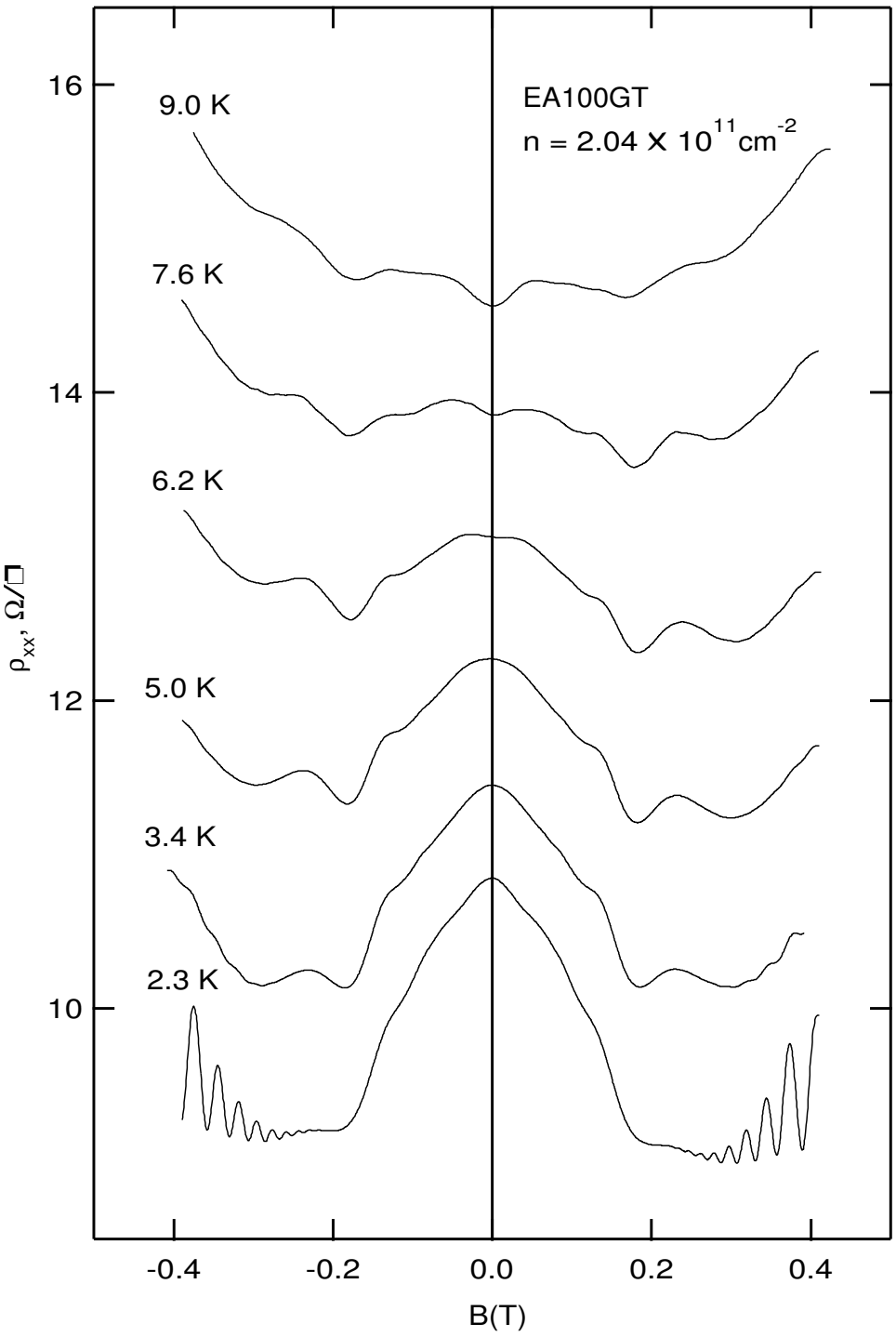

Figure B.4. Temperature dependence of magnetoresistance oscillations in EA100GT

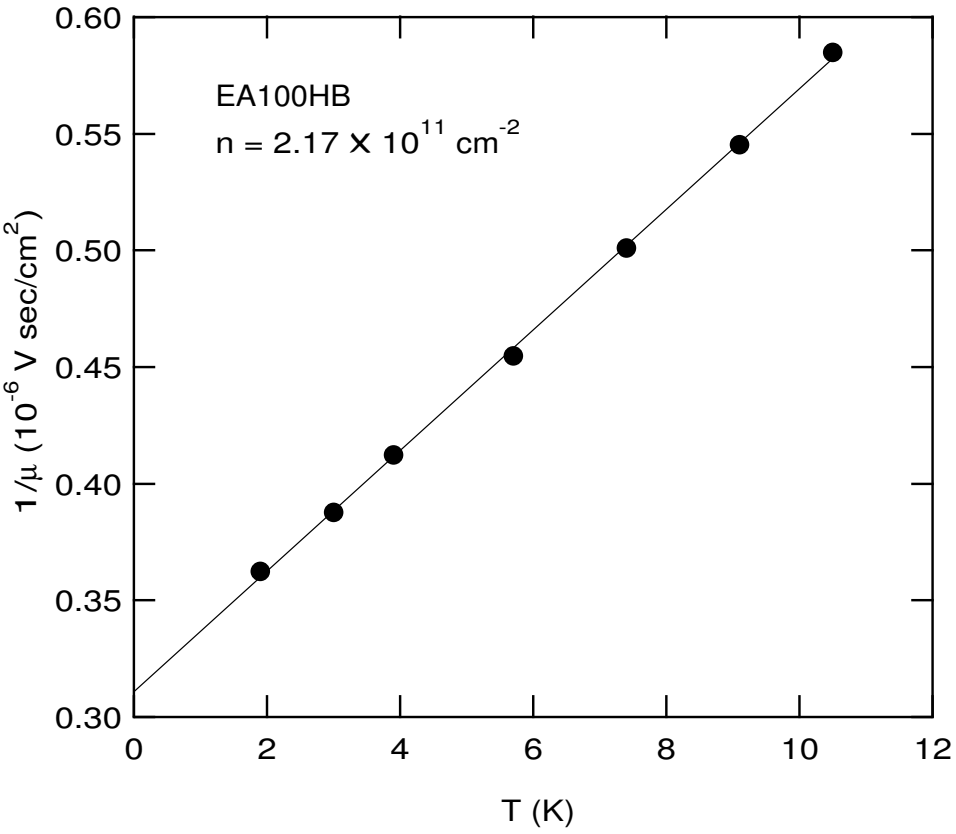

Figure B.5. Temperature dependence of inverse mobility

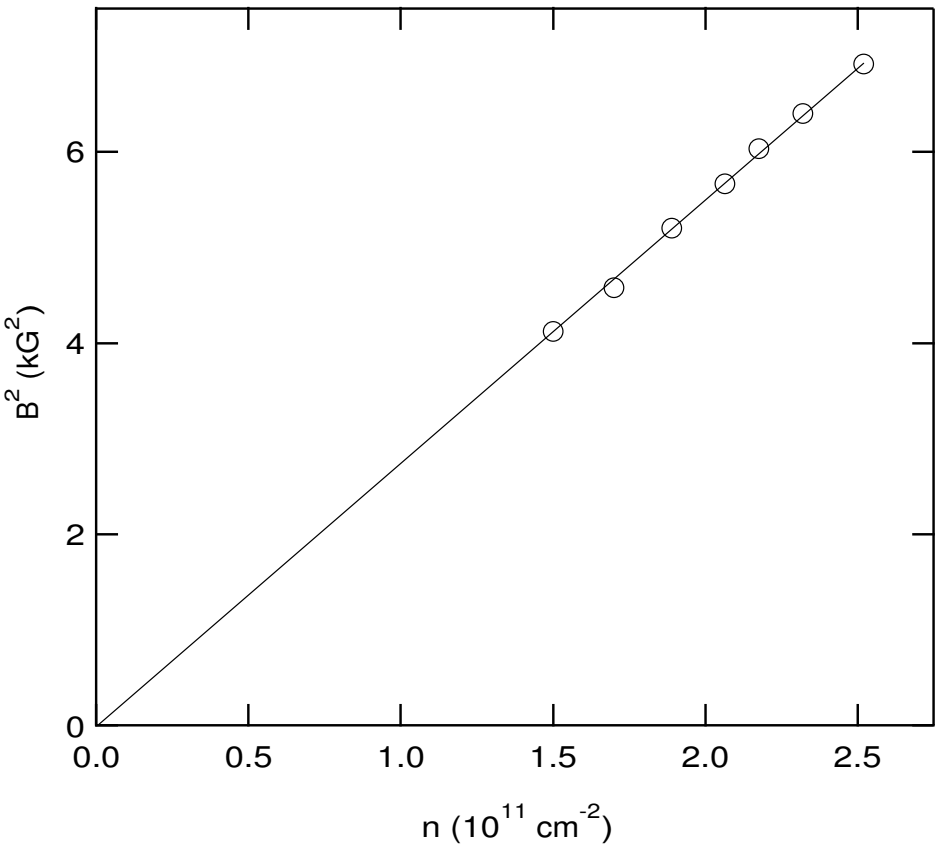

Figure B.6. Density dependence of the magnetic field corresponding to lowest order oscillation

REFERENCES

[1] K. von Klitzing, G. Dorda, and M. Pepper, Phys. Rev. Lett. **45**, 494 (1980).

[2] D. C. Tsui, H. L. Stormer, and A. C. Gossard, Phys. Rev. Lett. **48**, 1559 (1982).

[3] *The Quantum Hall Effect*, ed. by T. Chakraborty and P. Pietilainen, Springer-Verlag, Berlin, 1995.

[4] *Perspectives in Quantum Hall Effect - Novel Quantum Liquids in Low-Dimensional Semiconductor Structures*, ed. by S. Das Sarma and A. Pinczuk, Wiley and Sons, New York, 1997.

[5] J. K. Jain, Phys. Rev. Lett. **63**, 199 (1989); J. K. Jain, Phys. Rev. B **41**, 7653 (1990).

[6] B. I. Halperin, P. A. Lee, and N. Read, Phys. Rev. B **47**, 7312 (1993).

[7] D. Weiss, M. L. Roukes, A. Menschig, P. Grambow, K. von Klitzing, and G. Weimann, Phys. Rev. Lett. **66**, 2790 (1991).

[8] W. Kang, H. L. Stormer, and L. N. Pfeiffer, Phys. Rev. Lett. **71**, 3850 (1993).

[9] V. J. Goldman, B. Su, and J. K. Jain, Phys. Rev. Lett. **72**, 2065 (1994).

[10] J. H. Smet, D. Weiss, R. H. Blick, G. Lutjering, K. von Klitzing, R. Fleischmann, R. Kethmerick, T. Geisel and G. Weimann, Phys. Rev. Lett. **77**, 2272 (1996).

[11] R. L. Willett, R. R. Ruel, K. W. West, and L. N. Pfeiffer, Phys. Rev. Lett. **71**, 3846 (1993).

[12] R. R. Du, H. L. Stormer, D. C. Tsui, L. N. Pfeiffer, and K. W. West, Phys. Rev. Lett. **70**, 2944 (1993).

[13] R. R. Du, H. L. Stormer, D. C. Tsui, A. S. Yeh, L. N. Pfeiffer, and K. W. West, Phys. Rev. Lett. **73**, 3274 (1994).

[14] G. Abstreiter, J. P. Kotthaus, J. F. Koch, and G. Dorda, Phys. Rev. B **14**, 2480 (1975).

[15] M. J. Chou, D. C. Tsui, and G. Weimannn, Phys. Rev. B **37**, 848 (1988).

[16] S. J. Allen, Jr., D. C. Tsui, and R. A. Logan, Phys. Rev. Lett. **38**, 980 (1977).

[17] T. N. Theis, Surf. Sci. **98**, 515 (1980).

[18] E. Batke, D. Heitmann, and C. W. Tu, Phys. Rev. B **34**, 6951 (1986).

[19] *Landau Level Spectroscopy*, ed. by G. Landwehr and E. I. Rashba, Elsevier Science Publishers, North-Holland, 1991.

[20] C. C. Li, L. W. Engel, D. Shahar, D. C. Tsui, and M. Shayegan, Phys. Rev. Lett. **79**, 1353 (1997).

[21] B. E. Cole *et al*, Phys. Rev. B **55**, 2503 (1997).

[22] M. Dobers, K. v. Klitzing, and G. Weimann, Phys. Rev. B **38**, 5453 (1988).

[23] M. E. Raikh *et al.*, unpublished (1997).

[24] T. Ando, A. Fowler, and F. Stern, Rev. Mod. Phys. **54**, 437 (1982).

[25] L. Shubnikov and W. J. de Haas, Leiden Comm. 207a, 207c, 207d, 210a (1930).

[26] E. N. Adams and T. D. Holstein, J. Phys. Chem. Solids **10**, 254 (1959).

[27] R. B. Dingle, Proc. Roy. Soc. (London) A **211**, 517 (1952).

[28] *e.g.* P. T. Coleridge, R. Stoner, and R. Fletcher, Phys. Rev. B **39**,1120 (1989); P. T. Coleridge, Phys. Rev. B **44**, 3793 (1991).

[29] R. B. Laughlin, Phys. Rev. Lett. **50**, 1395 (1983).

[30] F. D. M. Haldane, Phys. Rev. Lett. **51**, 605 (1983).

[31] B. I. Halperin, Phys. Rev. Lett. **52**, 1583 (1984); **52**, 2390(E) (1984).

[32] R. R. Du, A. S. Yeh, H. L. Stormer, D. C. Tsui, L. N. Pfeiffer, and K. W. West, Phys. Rev. Lett. **75**, 3926 (1995).

[33] R. R. Du, A. S. Yeh, H. L. Stormer, D. C. Tsui, L. N. Pfeiffer, and K. W. West, Surf. Sci. **361/362**, 26 (1996).

[34] Frank Stern, Phys. Rev. Lett. **18**, 546 (1967).

[35] K. W. Chiu and J. J. Quinn, Phys. Rev. B **9**, 4724 (1974).

[36] G. Eliasson, J.-W.Wu, P. Hawrylak and J. J. Quinn, Solid State Comm. **60**, 41 (1986).

[37] T. Ando, J. Phys. Soc. Jpn., **38**, 989 (1975).

[38] A. Pinczuk, B. S. dennis, L. N. Pfeiffer and K. W. West, Phys. Rev. Lett. **70**, 3983 (1993).

[39] W. Walukievicz, H. E. Ruda, J. Lagovski, and H. C. Gatos, Phys. Rev. B **30**, 4571 (1984).

[40] E. E. Mendez, P. J. Price, and M. Heiblum, Appl. Phys. Lett. **45**(3), 294 (1984).

[41] H. L. Stormer, L. N. Pfeiffer, K. W. Baldwin, and K. W. West, Phys. Rev. B **41**, 1278 (1990).

[42] D. Weiss, M. L. Roukes, A. Menschig, P.Grambow, K. von Klitzing, and G.Weinmann, Phys. Rev. Lett. **66**, 2790 (1991).

[43] T.Yamashiro, J. Takahara and Y. Takagaki, Solid State Comm. **79**, 885 (1991).